Advances in numerical modelling of swash zone dynamics

note finali coverpage

(Article begins on next page)

28 August 2024

Advances in numerical modelling of swash zone dynamics

Riccardo Briganti[a,*], Alec Torres-Freyermuth[b], Tom E. Baldock,[c], Maurizio Brocchini,[d], Nicholas Dodd,[a], Tian-Jian Hsu,[e], Zhonglian Jiang,[c], Yeulwoo Kim,[e], Jose Carlos Pintado-Patiño,[b,f], Matteo Postacchini[d]

[a]*Coastal Dynamics and Engineering Group, Infrastructure and Geomatics Division, Faculty of Engineering, University of Nottingham, Nottingham NG7 2RD, U.K.*
[b]*Laboratorio de Ingeniería y Procesos Costeros, Instituto de Ingeniería, Universidad Nacional Autónoma de México, Sisal, Mexico*
[c]*School of Civil Engineering, University of Queensland,Brisbane, QLD, 4072, Australia.*
[d]*Università Politecnica delle Marche, Department of Civil and Building Engineering and Architecture (DICEA), Italy*
[e]*Center for Applied Coastal Research, Civil and Environmental Engineering, University of Delaware, Newark, DE 19716*
[f]*Programa de Maestría y Doctorado en Ingeniería, Universidad Nacional Autónoma de México, DF 04510, México*

Abstract

We present a comprehensive and critical review of work on the numerical modelling of swash zone processes between 2005 and 2015. A wide range of numerical models has been employed for the study of this region and, hence, only phase-resolving approaches (i.e., depth-averaged and depth-resolving models) are analyzed. The current advances in the modelling of swash zone processes are illustrated by comparing different numerical models against laboratory experiments of a dam-break-driven swash event. Depth-averaged and depth-resolving models describe well the swash flow for both coarse sand and gravel impermeable beach cases. Depth-averaged models provides a practical tool for engineering use, whereas depth-resolving models improve the flow description, especially for the backwash phase, with a significantly higher computational cost. The evolution and magnitude of bed shear stresses predicted by all models is rea-

sonable when compared with laboratory estimates based on the log-law. However, differences between modelling approaches cannot be rigorously evaluated owing to the uncertainty in shear stress estimates while employing such approximation. Furthermore, small-scale processes, such as turbulence evolution, are investigated with depth-resolving models, finding differences between the two-dimensional and three-dimensional approaches. Numerical models allow us to investigate other processes such as beach morphology changes, the evolution of the turbulence coherent structures, and the infiltration/exfiltration effects on the swash flow. A discussion on the advantages and limitations of each model is presented. The future of swash zone modelling depends on the increase of the computational power and, more importantly, on the improvement of the current capability to obtain intra-wave measurements for model validation, calibration, and greater resolution of physical processes.

1. Introduction

The beach region alternatively covered and uncovered by the short and long wave-induced water level fluctuations is known as the swash zone. The understanding of this region is fundamental to predict beach erosion and inundation during both extreme and mean wave conditions. Furthermore, it can be expected that the effects of climate change (e.g., sea level rise and storm intensification) will produce a more drastic impact on this region of the foreshore. However, the investigation of the physics of the transient, shallow, turbulent and multi-phase swash flow is a challenge for the fluid mechanics, because conducting measurements in this region is very difficult (Puleo et al., 2012). Therefore, the numerical modelling of the swash zone dynamics has been the focus of active research during the past decade (see Brocchini and Baldock, 2008).

The 1st International Workshop On Swash Zone Processes (Puleo and Butt, 2006) that took place in 2004, provided guidance regarding to where swash

dynamics research efforts should be directed. During the meeting, some of the key topics on the hydrodynamics and sediment transport that needed to be addressed were identified. These topics included: the spatio-temporal structure of velocity profiles and turbulence, the boundary layer dynamics, the effect of infiltration/exfiltration on sediment transport within the swash zone, and the modelling of morphological changes.

The aim of the present contribution is twofold. On one hand, the paper aims at presenting a comprehensive review of work on swash zone processes modelling published in the decade 2005-2015 (Section 2). In ten years a wide range of numerical models have been used in the context of swash processes and hence we focus only on the intra-wave (phase-resolving) approaches. On the other hand, we critically analyze the ongoing work by comparing different models through a specific, representative, benchmark case of dam-break-driven swash experiments. A general description of the depth-resolving and depth-averaged models employed in this work is given in Section 3. The different phase-resolving models are compared with the benchmark case and are further employed to investigate other processes in Section 4. This is followed by a discussion on the models capabilities/limitations based on the results from the previous section (Section 5). Finally, concluding remarks are presented in Section 6.

2. The recent past: review of swash zone modelling

Swash zone modelling efforts using phase-resolving models have been devoted to improve the knowledge of intra-swash flow and bed evolution. Here, a review of recent work related to these topics is presented. The approach here followed is that of describing the hydrodynamics moving in the surface-to-bottom direction and the morphodynamics from the small-scales to the large-scales.

2.1. Description of the flow

2.1.1. Flow velocity, turbulence, acceleration

The detailed and accurate description of the flow structure at any stage of bore generated swash events (i.e., bore shoaling, collapse, run-up and down-

3

rush) is of paramount importance for the knowledge of swash processes and, in particular, for the understanding of the interaction between the flow and the sediment. Numerical models based on depth-resolving equations are best suited to provide an insight in the flow structure and they contributed in describing features of such flow at scales so small that cannot be resolved with experimental methods. The resolution of these features and the description of the evolution of flow parameters and turbulence are among the most significant advances in the knowledge of swash flows of the last decade.

Zhang and Liu (2008) provided a comprehensive analysis of a bore-generated swash event using Reynolds-Averaged Navier Stokes (RANS) equations, which has been verified and further extended by subsequent studies. The evolution of the flow in the shoaling region depends on the bore strength, i.e. by its Froude number. Stronger bores are those that break during the shoaling phase, before arriving at the undisturbed position of the shoreline, whereas weaker bores collapse only when they reach the still-water shoreline. The offshore flow parameter hence determines important differences in the other phases of the flow (as also found by Guard and Baldock, 2007) and, in particular in the evolution of the Turbulent Kinetic Energy (TKE). In the strong-bore case the TKE is produced only at bore breaking when the production/dissipation of TKE are roughly in balance. Further up the beach, the TKE undergoes a power-law decay with a 1.3 slope, similar to homogenous grid turbulence. For the weak-bore case the maximum TKE occurs at the beginning of the run-up phase and the TKE decay rate is only half of that occurring at a strong bore. This description of the evolution of the TKE has been confirmed in the subsequent works of Bakhtyar et al. (2009) and Desombre et al. (2013).

After the collapse the run-up phase begins and, as the swash lens stretches on the beach, the velocity profile becomes uniform on the water column and the speed of the tip decreases owing to the effect of the bottom stress. One of the most important small-scale features resolved by Zhang and Liu (2008) is a secondary mini-bore collapse that occurs in the late stage of the run-up in the strong bore case. This was later observed in the laboratory experiments by

4

Kikkert et al. (2012).

The later stages of run-up and the occurrence of flow reversal are critical for the development of the bottom boundary layer (see subsection 2.1.2) and hence for sediment transport. Depth-resolving models predict that at this stage the vertical structure of the velocity is complex. Reversal starts away from the tip of the swash lens and from the bottom of the water column. This creates velocity profiles similar to those of a strong wall-jet (Zhang and Liu, 2008). However, the implication of these features on sediment transport are not yet determined and numerical models that predict bed evolution (e.g., Briganti et al., 2012) do not currently take this into account.

As the backwash progresses the flow velocity increases and at a later stage the surface forms a bore-like feature, approximately at the position of the still-water shoreline, confirming the onset of a backwash bore discussed in the early work of Hibberd and Peregrine (1979). This feature is also well captured by virtually all models used for swash flows and discussed here. TKE levels in the backwash are much lower than in the uprush and are bed-generated. Together with the dynamics of the TKE, flow accelerations during a swash event have been extensively studied in the last decade as a likely primary agent of enhanced onshore sediment transport. However, shoreward-directed accelerations exist only for up to 22% of the swash cycle, hence, as found in Puleo et al. (2007), using again a RANS model. Hence, the aforementioned enhancement occurs only for a short duration. The description of the acceleration provided by Puleo et al. (2007) was also confirmed by O'Donoghue et al. (2010) who used a Non Linear Shallow Water Equations (NLSWE) solver. Furthermore, near bed pressure gradients are poorly correlated to the local fluid acceleration. Further studies (Torres-Freyermuth et al., 2013) suggested that an acceleration-enhanced sediment transport formulation does not improve sediment transport prediction within the swash zone.

2.1.2. Bottom boundary layer dynamics

Beyond the fundamental dynamics that evolve within the water body, the evolution of the Bottom Boundary Layer (BBL) and, in turn, that of the bed shear stress, during a swash event plays an important role in sediment transport. One of the most important issues highlighted by Puleo and Butt (2006) was the need to overcome the formulation of the shear stress based on steady flow results. To this end, numerical models based on NLSWE have been used in conjunction with simplified BBL models to provide a simple yet accurate estimates of the bottom shear stress.

The development of the BBL is impulsive at bore arrival and it quickly becomes depth-limited until the flow slows down and approaches reversal. During the backwash phase the BBL grows again to become depth limited. This description was achieved by using the momentum integral method by Barnes and Baldock (2010) and Briganti et al. (2011) who employed a Lagrangian and Eulerian framework, respectively. These two studies indicated that the momentum integral method provides a reasonable description of the BBL during the uprush, while the accuracy of the models decreases for the backwash. However, details, e.g. that flow reversal occurs close to the bottom first (see Zhang and Liu, 2008), are not captured by these models. Furthermore, the impulsive development of the BBL in the uprush may not be the result of turbulent diffusion; its growth might be explained also with the horizontal straining of fluid parcels associated with the bore arrival (Torres-Freyermuth et al., 2013, Pintado-Patiño et al. (2015)). Therefore, the validity of the momentum integral method needs to be assessed. As a consequence of the evolution of the BBL, the landward-directed bed shear stress is maximum during the early stage of run-up, in correspondence of the bore collapse (see Barnes and Baldock, 2010 and Briganti et al., 2011). At different locations, the magnitude of the stress is maximum at the arrival of the water front and rapidly decreases, becoming negligible around flow reversal. During the backwash the stress, now directed seaward, increases in magnitude until it reaches a maximum, after which it decreases until the swash event ends.

6

2.1.3. The role of infiltration/exfiltration

Moving from within the water region to the top layer of the seabed the infiltration (and exfiltration) of the water into (and out from) the bed has an impact on momentum balance and swash sediment transport. The interaction between the flow above the beach and that below was extensively studied using both experimental and numerical methods. These latter helped in clarifying the exchanges between the porous beach face and the groundwater. For an unconfined coastal aquifer these exchange occur both in the surf zone and in the swash zone. Wave breaking and infiltration/exfiltration increase the hydraulic gradient across the beach face, inducing infiltration before the breaking point and exfiltration just in correspondence of the breaking point (Bakhtyar et al., 2011). Infiltration is strong in the swash zone, above all in the upper part of the beach. The maximum infiltration rates occur when the water table is lower than the mean water level under coarser sediment conditions, in which the beach accretion is promoted (Bakhtyar et al., 2011).

If the beach is unsaturated, the infiltrating swash flow interacts with air. The numerical study by Steenhauer et al. (2012) models the behaviour of the two phases during swash events on a coarse sand and a gravel beaches. For the coarse sand case, during the uprush a strong air pressure, build up below the wetting front, hampers infiltration. The hydraulic gradient then becomes negative causing exfiltration during the backwash. On the other hand, in the gravel bed case the pressure build up is weaker, allowing faster infiltration and bed saturation rates.

The direct effect of infiltration/exfiltration on the sediment transport is very complex. Three different mechanisms impact on sediment transport (Baldock and Nielsen, 2010): (1) the effect on bed shear stress through a modified free stream and thinning/thickening of the BBL; (2) the effect on immersed particle weight as used in the Shields parameter; and (3) the effect on the threshold of motion, as given by the critical Shields number. Numerical studies allowed

7

to identify how these mechanisms depend on the sediment size. The effective weight reduction dominates over BBL modifications for finer sediments (i.e., $D_{50} = 0.2$ mm, as indicated by Hoque and Asano, 2007), enhancing offshore net sediment transport. Contrarily, for coarser grains (i.e., D_{50} larger than 0.6 mm, according to Karambas, 2003, Karambas, 2006 and Hoque and Asano, 2007), the BBL modifications dominate over reductions in the effective weight of particles and promotes an onshore net sediment transport. The numerical study by Pintado-Patiño et al. (2015) further suggests that the effect of infiltration and exfiltration can be so strong that it dominates over BBL development and hence flat plate boundary layer theory, applied in the studies mentioned in Section 2.1.2, may not be applicable under some conditions.

2.2. Description of bed evolution

2.2.1. Sediment transport

During the last decade the knowledge of the sediment transport within a single swash event improved thanks to both experimental and numerical studies (Chardón-Maldonado et al., 2016). For instance, numerical models have clarified the role of bore collapse in mobilising and advecting sediments into the swash zone. Immediately after bore arrival the sediment concentration increases impulsively, together with the sheet flow thickness. During this initial phase of the swash event, the bore turbulence contributes significantly to sediment suspension and to advection of pre-suspended sediments from the inner surf zone into the swash zone. The bore turbulence effect on sediment mobilization is significant when turbulence reaches the bed. This occurs when the ratio between the bore height and local water depth is greater than 0.5 (Hsu and Raubenheimer, 2006), implying that suspended sediments at bore arrival originate from outside the swash zone (Calantoni et al., 2006, Hsu and Raubenheimer, 2006, Alsina et al., 2009). The process of advection of sediments into the swash zone is so important that it controls both the transport pattern and the net erosion/accretion on the beach face (Pritchard and Hogg, 2005). The zone in which sediments are picked up is found to extend seaward to a depth

approximatively equal to the bore height . The sediment advection length, i.e. its excursion during a swash event, depends on the type of breaker occurring at bore collapse but it is bound to 0.5 times the run-up length (Baldock et al., 2008). The maximum sediment load occurs at bore collapse and, further up the beach the concentration diminishes and lags behind the tip of the swash length (Alsina et al., 2009). Note that Pritchard and Hogg (2005), Baldock et al. (2008) and Alsina et al. (2009) all used Lagrangian models based on NLSWE that allowed an analysis of the trajectories of water particles from the surf into the swash zone that were used as proxies for sediment trajectories.

The use of single- and two- phase depth-resolving models (Hsu and Raubenheimer, 2006) suggested that sediment transport is in phase with the bottom stress, hence the total sediment load can be parametrised with Meyer Peter and Müller (MPM) formula, or its derivates (Othman et al., 2014), commonly used in coastal morphodynamic models (e.g., Incelli et al., 2015). Parametrizations of the sediment transport rate for sheet flow regimes have been proposed using two-phase models (Hsu and Hanes, 2004, Amoudry et al., 2008 and Amoudry and Liu, 2010), but at the moment they have not been implemented in NLSWE models.

2.2.2. Swash morphodynamics

The evolution of the beach face within a swash cycle is extremely difficult to measure (Chardón-Maldonado et al., 2016). Thus, numerical models provided a very valuable insight in the intra-swash bed changes. Here, hydromorphodynamic models are referred as fully-coupled if the flow and the bed evolution equations are solved simultaneously. This implies that the eigenvalues of the system should be computed at each time step (e.g., Kelly and Dodd, 2009, 2010; Xiao et al., 2010; Briganti et al., 2012; Zhu et al., 2012; Zhu and Dodd, 2013, 2015; Hu et al., 2015). On the other hand, weakly-coupled models solve the flow and bed equations sequentially at each time step (e.g., Postacchini et al., 2012; Kim, 2015; McCall et al., 2015). Typically, the bed evolution equations used are sediment conservation equations , such as the Exner equation.

9

Note that most of the previous works use depth-integrate hydrodynamic equations, while the use of depth-resolving equations is very limited (e.g., Bakhtyar et al., 2011).

Numerical models that solved the NLSWE-Exner system using the Method of Characteristics provided a detailed description of intra-swash bed evolution for idealised bore-driven swash (e.g., Peregrine and Williams, 2001) in the case of bed load only (Kelly and Dodd, 2010) and in presence of suspended load also (Zhu and Dodd, 2015). For bed load only, immediately after the dam-break a large quantity of sediment is mobilised at the tip (see Section 2.2.1), erosion is generated at the dam break point, where sediment is picked-up and as the flow slows down in the later stage of run-up the sediment is distributed along the beach. During the backwash the fast, supercritical flow erodes the beach. However, the predicted final bed profile depends on the coupling used. For instance, fully-coupled models predict a net bed erosion after the event, while uncoupled ones predict accretion in the upper part of the beach (Kelly and Dodd, 2010). Weakly-coupled models predict a final bed that is close to that predicted by fully-coupled ones (Postacchini et al., 2012). In particular the simulation of the bed evolution during the uprush by the two classes of models is very similar, except in the region of bore collapse (Postacchini et al., 2014).

The net bed change depends on the relative importance of the suspended load (e.g., Zhu and Dodd, 2015). For instance, when the suspended load is dominant over the bed load, accretion is predicted in the upper part of the beach and erosion in the lower part. Moreover, re-suspended sediment was found to increase the deposition at the base of the swash.

A more realistic swash event is that of a solitary wave. Its uprush phase is qualitatively similar to that of the Peregrine and Williams (2001) case (Zhu and Dodd, 2015). However, in the backwash a bed step, associated with a backwash bore, is formed below the still water level at the end of the swash event and the suspended load has only a slight influence on this process.

Numerical studies of multiple swash events aimed at improving the capabilities to achieve qualitatively-accurate predictions of the bed evolution under realistic

conditions. As expected, the parameterisation of the bed friction was central in these studies. A variable friction factor was used in the Chezy formulation of the bottom friction in Pedrozo-Acuna et al. (2006) noting that this improved the prediction of beach profiles. This is an heuristic approach to take into account several physical processes (i.e. the effects of infiltration, asymmetry in acceleration, differences in the evolution of the BBL in each phase of the swash and the effect of the plunging breaker at bore collapse) that are not incorporated in the numerical model. Nevertheless, when this approach was extended to mixed gravel and sand beaches (Pedrozo-Acuña et al., 2007), the quantitative agreement of the prediction was not satisfactory, in particular for mixed beaches. More recent studies separated the parameterisation of physical processes overcoming many limitations of these earlier models. Infiltration/exfiltration and acceleration on gravel beaches are treated explicitly in McCall et al. (2015), showing the importance of the subsurface processes in improving the accuracy of morphodynamic modelling of gravel beaches. Infiltration was considered also for sandy beaches in conjunction with the momentum integral method for bottom friction in Incelli et al. (2015). The study showed how quantitative agreement with measurement depends greatly on the availability of suitable boundary conditions of hydrodynamic parameters and sediment transport and not only on the parametrisation of physical processes.

3. State-of-the-art numerical models

After a review of the main contributions to swash zone understanding we move to a critical inspection of models that are currently used for the same task. Hence, the following section provides a description of the governing equations and assumptions of such models and the detail of the specific solvers chosen for our analysis. These models will be compared against laboratory experiments of dam-break-driven swash in Section 4 and will be further employed to investigate the processes occurring within a swash event that were not resolved in laboratory

11

experiments.

3.1. Depth-resolving models

Swash zone flows can be regarded as incompressible flows of a Newtonian
fluid, hence, the fundamental governing equations describing the flow in this
region are the well-known Navier-Stokes equations. However, swash flows typi-
cally evolve at very high Reynolds numbers being almost always turbulent and
making the Direct Numerical Solution (DNS) of Navier-Stokes equations impos-
sible due to the extremely large computational efforts required to resolve the
smallest scale of turbulence. Therefore, a range of simplified approaches can
be adopted to reduce the degree of freedom in such highly nonlinear system.
We here briefly discuss both the Large-Eddy Simulation (LES) and the RANS
approaches.

In LES models the large-scale energy-containing eddies are resolved while
the evolution and dissipation of smaller-scale eddies are parameterized with
closure models (e.g., Meneveau and Katz, 2000). Filtering over the Navier-
Stokes equations is used to decompose the velocity field into resolved and sub-
grid (un-resolved) component. The filter length scale is typically chosen to be
the grid size. Large-scale motions, which are greater than the filter length, are
directly resolved by the filtered Navier-Stokes equations given by,

$$\frac{\partial \bar{u}_i}{\partial x_i} = 0 \tag{1}$$

$$\frac{\partial \bar{u}_i}{\partial t} + u_j \frac{\partial \bar{u}_i}{\partial x_j} = -\frac{1}{\rho} \frac{\partial \bar{p}}{\partial x_i} + \nu \frac{\partial^2 \bar{u}_i}{\partial x_i \partial x_j} + g_i + \frac{\partial \tau_{ij}}{\partial x_j} \tag{2}$$

where i, j=1, 2, 3 for three-dimensional flow and the overbar denotes filtering.
The filtered velocity and pressure are $\bar{u}_i$ and $\bar{p}$, respectively. The kinematic
viscosity is denoted by ν, ρ is the fluid density, $g_i = (0, 0, -g)$ is the gravitational
acceleration, and τ_{ij} is the sub-grid stress tensor, which requires further closure
models. Although much more computationally efficient than DNS, LES still
requires a time-dependent three-dimensional (3D) Navier-Stokes solver because

12

turbulent eddies are always transient and three-dimensional. Moreover, the grid size needs to be sufficiently small, such that significant amount of turbulent energy in the inertial sub-range is resolved.

To further reduce the degree of freedom in the Navier-Stokes system, one can resolve only the ensemble-averaged mean flow field while parameterizing all the scales of turbulent fluctuations. Under this assumption, a coarser grid size can be used to resolve the mean flow. More importantly, if the flow can be considered statistically homogeneous in a given direction, one can solve a set of two-dimensional (2D) equations. This allows a significant reduction of computational effort compared to LES. By carrying out Reynolds decomposition, where the velocity and pressure are separated into the ensemble-averaged mean flow (represented by angle bracket $\langle\rangle$ and turbulent fluctuations (represent by prime $'$), and applying Reynolds-averaging over the Navier-Stokes equations, one obtains the so-called RANS equations which are written as,

$$\frac{\partial \langle u_i \rangle}{\partial x_i} = 0 \tag{3}$$

$$\frac{\partial \langle u_i \rangle}{\partial t} + \langle u_j \rangle \frac{\partial \langle u_i \rangle}{\partial x_j} = -\frac{1}{\rho}\frac{\partial \langle p \rangle}{\partial x_i} + g_i + \frac{1}{\rho}\frac{\partial \langle \tau_{ij} \rangle}{\partial x_j} - \frac{\partial \langle u_i' u_j' \rangle}{\partial x_i} \tag{4}$$

where $\langle u_i' u_j' \rangle$ is the Reynolds stress, which requires further closure models.

The LES and RANS approaches discussed so far are fairly general. A variety of models based on LES and RANS has been developed to describe the wave transformation but may be different from each other due to closures, numerical schemes, and boundary conditions (e.g., free-surface tracking method and bottom wall models). Such numerical models allow for a detailed description of the flow including turbulence quantities and the modelling of flow infiltration/exfiltration. A general description of the LES and RANS models employed here are given below.

3.1.1. Large-eddy simulation (LES)

We here use the open-source finite-volume Computational Fluid Dynamics (CFD) toolbox, OpenFOAM (www.openfoam.org). Among the various solvers

13

within the OpenFOAM, we utilized an incompressible Navier-Stokes equations solver for two immiscible fluids, called interFOAM (Klostermann et al., 2013; Rusche, 2002) and incorporate minor modification in a bottom boundary condition for rough bed based on the log-law. Recently, Zhou et al. (2014) validated this LES solver with the laboratory experiment from Ting (2006, 2008) for a solitary spilling breaker over a slope. The unresolved sub-grid scale motion is parameterized by the standard Smagorinksy closure, where a sub-grid eddy viscosity is used with a Smagorinsky coefficient of 0.167. The Volume of Fluid (VOF) method is used to track the free surface (Hirt and Nichols, 1981; Klostermann et al., 2013). The convection term is converted into surface integrals for each cell using Gauss theorem. Then, cell-fluxes are calculated with the flux limiter of the Total Variation Diminishing (TVD) scheme (Berberovi et al., 2009); more detailed discussion on the model formulation and numerical scheme can be found in Zhou et al. (2014).

3.1.2. Reynolds-Averaged Navier Stokes equations (RANS) model

The 2DV RANS model, called Cornell Breaking Wave and Structures (CO-BRAS; Lin and Liu, 1998a; Losada et al., 2008) is here used. The Reynolds stress tensor is calculated by the eddy viscosity and strain rate of the mean flow (Lin and Liu, 1998a; Shih et al., 1996). The eddy viscosity is computed by solving the balance equation of TKE (κ) and turbulent dissipation rate ϵ, namely, the well-known $\kappa - \epsilon$ model. The numerical solution of the RANS equation in COBRAS is based on the finite difference scheme with the two-step projection method (Lin and Liu, 1998b). Similarly, VOF method (see Hirt and Nichols, 1981) is used to track the free surface and the log-law for the bed-parallel velocity is prescribed at the bottom. The bed-orthogonal velocity is zero at the bed. The bed-parallel velocity at half the first grid point above bed ($\Delta z/2$) is used to determine the friction velocity ($u_\star$). The components of the velocity at higher grid points in the water column are solved numerically (Lin and Liu, 1998a). Additionally, the so-called Volume-Averaged/Reynolds Averaged Navier-Stokes (VARANS) equations can be used to model the flow properties

14

inside a porous media. The set of equations are obtained by applying an in-
trinsic volume average to the RANS equations over a control volume that is:
(i) larger than the characteristic pore size, and (ii) smaller than the scale of
the physics involved (Hsu et al., 2002). Thus, the volume-averaged quantities
can be related to a Darcy and/or Forchheimmer type model in order to describe
the subsurface flow and momentum transfer terms at the bed interface (e.g., Liu
et al., 1999). The turbulence field in the porous media is similarly approximated
via the $\kappa - \epsilon$ balance, in which the closure model of Nakayama and Kuwahara
(1999) accounts for the additional sources of turbulence due to the porous el-
ements. Further details regarding the COBRAS-RANS model can be found in
Lin and Liu (1998a,b). The complete description of the COBRAS-VARANS
model is provided by Liu et al. (1999) and Hsu et al. (2002).

3.2. Depth-integrated models

Numerical models based on depth-integrated hydrodynamic equations have
had a prominent role in swash research for more than three decades (e.g. one of
the earliest work is Hibberd and Peregrine, 1979). A review of early works can be
found in Brocchini and Dodd (2008). These models can be distinguished into two
groups, whether they assume, or not, that the pressure is hydrostatic. NLSWE
stem from the assumption of hydrostatic pressure, on the other hand removing
this assumption leads to formulations such as Boussinesq-type equations or Non-
hydrostatic Shallow Water Equations. A general formulation is:

$$\frac{\partial \zeta}{\partial t} + \nabla \cdot \left[(\zeta + d) \right] \mathbf{U}_{\tilde{z}} = S_{cont,p} + S_{cont,sub} \qquad (5)$$

$$\frac{\partial \mathbf{U}_{\tilde{z}}}{\partial t} + \mathbf{U}_{\tilde{z}} \cdot \nabla \mathbf{U}_{\tilde{z}} + g \nabla \zeta = \mathbf{S}_{mom,p} + \mathbf{S}_f + \mathbf{S}_{turb} + \mathbf{S}_{body} + \mathbf{S}_{mom,sub}. \qquad (6)$$

where ζ is the free surface elevation, $\mathbf{U}_{\tilde{z}} = [u(x, y, \tilde{z}, t), v(x, y, \tilde{z}, t)]$ is the vector
of the horizontal velocity at a reference level $\tilde{z}$ with component $u(x, y, \tilde{z}, t)$ and
$v(x, y, \tilde{z}, t)$ along the x and y directions, respectively. d is the depth measured
at the Mean Water Level (MWL) and h is the total water depth $h = \zeta + d$
(see Figure 1 for a sketch of the variables). $S_{cont,p}$ is the term in the continuity

15

equations resulting from the non-hydrostic pressure, $\mathbf{S}_f$ is the bottom friction term, $\mathbf{S}_{turb}$ includes turbulent stresses, $\mathbf{S}_{mom,p}$ is the non-hydrostatic term in the momentum equation along x and y, and $\mathbf{S}_{body}$ represents dissipative body forces, the most important being those associated with wave breaking. Both are equal to zero in NLSWE. Non-hydrostatic pressure is assumed in two well-established approaches, Boussinesq-type models and non-hydrostatic NLSWE ones. In the former approach $S_{cont,p}$ and $\mathbf{S}_{mom,p}$ are both related to the frequency dispersion of waves, $\mathbf{U}_{\tilde{z}}$ is usually referred to $\tilde{z} = z_\alpha$ following Nwogu (1993). In the latter approach $S_{cont,p} = 0$, and $\mathbf{S}_{mom,p}$ are directly linked to the pressure function. If the pressure is taken as hydrostatic, the velocity is independent of $\tilde{z}$ and is the depth-avaveraged velocity:

$$\mathbf{U_z} = \overline{\mathbf{U}} = \frac{1}{\zeta + d} \int_h^\zeta \left[u(x, y, z, t), v(x, y, z, t) \right] dz. \tag{7}$$

NLSWE are the most commonly used depth-integrated equations for swash flows, as frequency dispersion of the incoming wave can be neglected. This occurs also in dispersive, hence non-hydrostatic models, which converge to NLSWE in the swash zone (e.g., Tonelli and Petti, 2012). NLSWE inherently model the propagation of bores, and they well describe bore-driven swash (Hibberd and Peregrine, 1979, Peregrine and Williams, 2001). The system of Eqs. (6) need closures to determine $\mathbf{S}_f$ and $\mathbf{S}_{turb}$, also other physical processes that occur during a swash event require coupling of the hydrodynamic equations with other models suitable to describe those processes. $\mathbf{S}_f$ is often expressed using an explicit relationship that links the stress to depth-averaged velocity (e.g. the Chezy formula, using a friction coefficient C_f in Postacchini et al., 2012, and the Manning bulk frictional force, using the resistance coefficient n in Hu et al., 2015). In few models (e.g. Briganti et al., 2011) τ_b is computed, at each time step, using the momentum integral method.

$S_{cont,sub}$ and $\mathbf{S}_{mom,sub}$ are the terms that, respectively, model the mass and momentum exchange with the subsurface flow. This requires an extra equation that models the subsurface hydrodynamics. Coupling is also used for the simu-

16

lation of bed evolution (e.g., with sediment conservation equations such as the Exner equation).

3.2.1. Briganti et al. (2011) and Briganti et al. (2012) models

The model proposed in Briganti et al. (2011) is a one-dimenstional depth-integrated (1DH) solver of the NLSWE based on a Godunov-Type, finite-volume scheme based on the Weighted Averaged Flux (WAF) TVD scheme. The NLSWE are solved in conservative form using uniform cells in which the variables are considered constant. The TVD technique assures that the scheme is shock capturing (see Toro, 1990 for details). $\mathbf{S_f}$ is treated together with the gravity term stemming from the conservative form of the NLSWE using a Strang operator splitting technique and the shoreline boundary conditions are prescribed according to the approach referred as Option 2b in Briganti and Dodd (2009). To compute $\mathbf{S_f} = \tau_b/\rho$ the momentum integral method is used. The bed shear stress is computed using the relationship $u_\star = \sqrt{\tau_b/\rho}$, where $u_\star$ is the friction velocity and is computed using Eq. (4) in Briganti et al. (2011). The same technique for the computation of τ_b is also employed in the Briganti et al. (2012) hydro-morphodynamic model that is also used here. This model solves the system of NLSWE and the Exner equation employing a simple McCormack scheme equipped with TVD capabilities following the approach of Garcia-Navarro et al. (1992). In the present paper, only the bed load (q_b) is considered, given the sediment size, using the MPM formula (Incelli et al., 2015).

3.2.2. Nielsen et al. (2005) NLSWE solver and Barnes and Baldock (2010) BBL model

Nielsen et al. (2005) proposed a two-dimensional depth integrated (2DH) NLSWE solver based on the shock capturing finite-volume technique of Zoppou and Roberts (1999). The model, called ANUGA, is released as an open source code (https://anuga.anu.edu.au). It uses tridiagonal cells and an approximate Riemann solver at the intercell boundaries. The Riemann problem is solved also at the wet-dry interface, where the characteristic speeds are modified ac-

cordingly. $\mathbf{S}_f$ is computed using the Manning resistance law. Furthermore, the numerical predictions of h and U have been applied as input conditions of the Lagrangian Boundary Layer Model (LBLM, Barnes and Baldock, 2010) to derive the evolution of the swash boundary layer. Particle trajectories are calculated by following the Eulerian-Lagrangian transformation (Alsina et al., 2009). The depth-averaged approach assumes no vertical motion and, therefore, each particle represents a fluid parcel covering $0 \leq z \leq h$. The Eulerian-Lagrangian transformation provides the flow history along the particle trajectories. The BBL evolution during a swash event is predicted using the integrated products of the fluid velocity and particle displacement along the trajectories. Prandtl's solution for the turbulent boundary layer growth is used for the computations of the BBL thickness δ. For the purpose of data-model comparison, a linear interpolation has been applied to derive the time series of predicted bed shear stress and BBL thickness at specified locations, i.e. in the Eulerian framework.

3.2.3. Postacchini et al. (2012) model

This weakly-coupled solver is based on the system made of the 2DH NLSWE, wave-resolving equations of conservation of mass and momentum and the Exner equation. Bottom friction is incorporated by means of a dimensionless friction coefficient C_f included in the common Chezy-type formulation, as described in Brocchini et al. (2001). Recently, the dissipative contribution induced by subgrid turbulence, i.e. evolving at smaller scales than the water depth, has been introduced (Postacchini et al., 2014). On the other hand, sediment fluxes and bed-level changes are calculated using standard sediment transport closures, many of which are implemented in the proposed solver to enable one to select the most appropriate for the analysed case. In the benchmark considered here only q_b is here modelled, using the bed load formula by Besio et al. (2003).

4. Ongoing research: A comparative analysis of a benchmark case

As a simple example of the state-of-the-art modelling of swash zone flows described in the previous sections, we here benchmark different types of solvers

18

on one single test case of a dam-break-driven swash event. The intent is both to show how different models simulate the processes described in Section 2 and to give a quantitative assessment of the models performance.

4.1. Description of the experiment (Kikkert et al., 2012)

The description of the experiment and results are explained in detail in Kikkert et al. (2012) and, hence, only a brief outline of the set-up is presented here. The swash facility and the experimental set up are shown in Figure 2. This was built into a flume that is 20 m long, 0.9 m high and 0.4 m wide. Its walls were made of glass to allow non-invasive optical investigations. At one end of the flume a water reservoir was present and a 1/10 rough impermeable sloping beach was located downstream of the gate of the reservoir. This was quasi-instantaneously lifted to generate the dam-break. The initial conditions of the experiment were: a water depth in the reservoir (h_d) of 0.6 m and water depth in front of the gate (h_0) of 0.062 m (Figure 2).

Three sediment sizes were tested to obtain different values of the bed roughness, ranging from coarse sand to gravel. Table 1 shows the target and effective D_{50} for the three experiments. Only the 1.5 mm coarse sand and 6.0 mm gravel tests are considered here. For each set of experiments, bed parallel velocity and depth were measured at six cross-shore locations, at 13.5 Hz, using a combined system of Particle Image Velocimetry (PIV) and Laser Induced Fluorescence (LIF), respectively. The locations of the centre of the PIV/LIF stations are reported in Table 2. The positions are referred to a frame of reference with the horizontal axis origin (x_0) located at the initial shoreline position in the experiment at 4.82 m from the gate (see Figure 2). Note that the x and z axes in the frame of reference for the PIV and LIF data (Figure 2) are not orthogonal. Ensemble avarages of hydrodynamic parameters were extracted from 50 repetitions of the same event. These data were, then, used to estimate the bed shear stress using various methods (see Kikkert et al., 2012). In the Table 2 the acronyms used for each location are reported, these are the same as in Briganti et al. (2011).

4.2. Setup of the numerical models

Numerical models described in Section 3 are employed in order to simulate the experimental conditions described in Section 4.1. Information on the mesh characteristics, boundary conditions, and computation time for each model are presented below. In particular we use two depth-resolving models (a LES and a RANS model) and three NLSWE solvers (Briganti et al., 2011, Nielsen et al., 2005 and the hydrodynamic module of Postacchini et al., 2012) to analyse the flow description. We also use two hydro-morphodynamic solvers (Briganti et al., 2012 and Postacchini et al., 2012) for the analysis of the bed evolution. Furthermore, a VARANS solver (e.g., Pintado-Patiño et al., 2015) is employed for the analysis of infiltration/exfiltration.

4.2.1. OpenFOAM LES model

A boundary fit-domain is constructed to model the dam-break experiment in the LES model. The numerical flume is of 10.9 m long, 0.45 m wide, and 0.65 m deep and the slope is identical to that used in the physical experiment. The model domain is discretized into 2480, 60, 90 grid points (for a total of 13.4 million points) in the streamwise (x), spanwise (y), and vertical (z) direction, respectively. All boundaries, except the top atmosphere region, are walls boundaries. For the rough sloping bed considered in this study, a near wall modelling approach is adopted. A non-uniform grid is applied in the vertical direction, with a minimum grid height of 0.0009 m near the bed. Time step of the computation is automatically adjusted by Courant-Friedrichs-Lewy (CFL) condition, resulting in a time step (Δt) of around 0.001 s. The numerical model is fully parallelized with Message Passing Interface, with the wall-clock time of the entire run being about 200 hrs using 48 processors.

4.2.2. COBRAS (Lin and Liu, 1998a) RANS model

For the RANS simulation, the sloping bathymetry is accommodated by solving the equations in a model coordinate system that is bed-parallel and bed-orthogonal (e.g., Puleo et al., 2007). The grid is irregular with a refined

sub-zone near the bed (from $z = 0$ m until $z = 0.3$ m) along the surf-to-swash transition until the end of the beach face slope (from $x = $ -1.01 m until $x = $ 5.01 m). The minimum grid cell size in this finer region are $\Delta x = 0.004$ m and $\Delta z = 0.003$ m. Therefore, the entire computational domain is composed of 81,1512 cells. The apparent roughness (k_s), needed to compute $u_\star$, is set equal to $k_s = 1.2D_{50}$ based on the optimization of the model skill. The time step is automatically adjusted during the computation to satisfy the stability constraints, i.e., Courant number. The computation time for a single simulation is of approximately 6 hrs using an Intel Xeon 2.53 GHz (6GB RAM) computer.

4.2.3. Briganti et al. (2011) and Briganti et al. (2012) models

The Briganti et al. (2011) model was used with the distance between the centre of two computational cells $\Delta x = 0.01$ m. The roughness factor for the beach (k_s), needed to estimate τ_b through the momentum integral method, is computed according to Engelund (1966), for the 1.5 mm coarse sand, resulting in $k_s = 0.0030$ and for the 6.0 mm, resulting in $k_s = 0.0120$, whereas for the fixed flat bottom in front of the beach $k_s = 0.0001$. Unlike in the original paper, where the boundary layer thickness (δ) was not limited, here δ has been imposed to be at most equal to h. The model was run with constant Courant number $Cr = 0.8$. For the simulation of bed evolution during the swash event, the fully-coupled hydro-morphodynamic model by Briganti et al. (2012) was used. The solver employed the same values for k_s and Δx of the aforementioned hydrodynamic model. For the Exner equation two parameters are needed, the porosity p and the relative density of the sediments s_{rel}. In the present application $s_{rel} = 2.65$ and $p = 0.4$ have been used. The Courant number used was $Cr = 0.4$. For the hydro- morphodynamic simulation of the event (with 10 s duration) the computation time is approximately 130 s on a standard PC (Processor: Intel (R) Core (TM) i3-2120 CPU @3.30GHz 3.30GHz; RAM: 4GB).

21

4.2.4. Nielsen et al. (2005) NLSWE solver and Barnes and Baldock (2010) BBL model

565   The flow is simulated using ANUGA for a complete dam-break, i.e. releasing the stationary reservoir of water into the stationary tailwater downstream. $\mathbf{S}_f$ is computed using the Manning resistance law in which the friction factor (n) is $n = 0.010$ for the horizontal portion of the flume and $n = 0.019$ for the sloping beach. These values (as well as C_f used in the following model) are

570   the results of a model calibration and produced the best results in terms of shoreline position and flow parameters. The maximum area of any triangle in the mesh is 0.001 m^2, $\Delta t = 0.02$ s. The boundary layer thickness and bed shear stress are calculated along the particle trajectories by incorporating the friction coefficient of rough bed conditions (Eq. 1 in White, 2006). The computation

575   time is approximately 170 s on a standard PC (Processor: Intel (R) Core (TM) i7-2600 CPU @3.40GHz 3.40GHz; RAM: 8GB).

4.2.5. Postacchini et al. (2012) model

Like for the other models the whole swash facility is simulated using the hydro-morphodynamic model by Postacchini et al. (2012). The model is here

580   used both for the simulation of the hydrodynamic only and the bed evolution. The following parameters have been used: $p = 0.4$, $s_{rel} = 2.65$ $C_f = 0.005$ in the horizontal portion of the flume and $C_f = 0.01$ on the sloping beach. Finally, $\gamma = 0.1$ (slope corrector). The hydrodynamical module of this model, which is essentially the Brocchini et al. (2001) WAF model, has been used to

585   simulate the fixed bed case for both the coarse sand and the gravel cases. The model has been run using $C_f = 0.01$ has been used for the coarse sand beach while $C_f = 0.015$ for the gravel beach. In both cases $C_f = 0.005$ is used on the horizontal portion of the swash flume. The computation time for a single (about 10 sec) simulation is of approximately 3 min, using an Intel Xeon Quad-core 2.53

590   GHz (6GB RAM) computer.

4.3. Model results

The numerical models described in Section 4.2 are employed to simulate the benchmark case described in Section 4.1. Model-data comparison is presented in order to highlight different models capabilities/limitations to simulate the different swash processes described in Section 2. Furthermore, we also analyzed the model performance to predict shoreline trajectory. Finally, the models capabilities to simulate additional swash zone processes that were not measured in the laboratory (i.e., beach morphodynamics and flow infiltration/exfiltration) are presented.

4.3.1. Shoreline position, water depth, flow velocity, and turbulence

Wave runup is important for coastal engineering applications. Thus, both depth-resolving and depth-integrated models are employed for computing the shoreline trajectory (x_s). The LES model overpredicts x_s rather significantly (see Figure 3a). The predicted shoreline position is sensitive to the threshold value used to define the wet-dry interface as well as to the sidewall boundary condition. In general, adopting near-wall modelling, especially for smooth walls, in LES requires high numerical resolution. It is likely that the spanwise grid size used here is too coarse to accurately model the sidewall effect. In the RANS model x_s is determined employing water depth equal to two cells (i.e., 6 mm) as a threshold because a residual film of one grid depth remain attached to the bed. The RANS model predicts the maximum shoreline position for the two cases (Figure 3a). In general, the shoreline trajectory is better simulated for the gravel beach case. Both the vertical grid resolution and the threshold value may affect the results significantly.

For the three NLSWE solvers the shorelines are plotted in Figure 3(b). All the three models predict the uprush phase, and the maximum run-up with good accuracy, with ANUGA showing the best performance. However, they differ more in the backwash phase (in both cases $h = 5$ mm identifies the shoreline). This difference is due to the different BBL models used, while the effect of the shoreline boundary condition is minimal (Briganti and Dodd, 2009).

23

Figures 4 and 5 show the depth-resolving models performance for the simulation of both water depth h and depth-averaged velocity U evolution of the swash event at three different cross-shore locations (PIV2, PIV4, and PIV5) for the sand and gravel beach, respectively. Similarly to the procedure used for the laboratory data, the depth averaged velocity U for the LES and RANS models is computed by averaging the velocity profiles at the PIV cross-shore locations. The LES model results are in better agreement with the data during bore arrival and discrepancies can be ascribed to air entrapment. High-frequency oscillations observed in the LES results are likely to be related to the technique employed to compute the ensemble estimate, i.e., spanwise averaging excluding 5 grid points next to the sidewalls. Differences between the sand and gravel beach case are more important at PIV5. The RANS model shows larger discrepancies for water depth during the bore arrival at PIV2 (Figures 4 and 5). These discrepancies might be ascribed to the RANS model over-prediction of turbulence. During bore arrival the depth-averaged velocity is overpredicted by the RANS model (Figures 4 and 5). In the backwash the agreement is good for both models for the sand case, while the LES model tends to overpredict the backwash peak velocity. The RANS model performance during the backwash on the gravel beach is excellent.

Depth-integrated numerical predictions of h and U are also shown for the coarse sand (Figure 6) and for the gravel (Figure 7) case at PIV2, PIV4 and PIV5. The visual comparison suggests a similar level of accuracy in the prediction of h and U across all models. ANUGA and Postacchini et al. (2012) show a better performance in the prediction of h in the upper part of the beach (PIV4 and PIV5) for the coarse sand. In this region Briganti et al. (2011) overpredicts h, above all during the backwash. All models predict the evolution of U during the uprush but mostly differ in the modelling at the later stages of backwash. Also, for the coarse sand, Briganti et al. (2011) overestimates U during the backwash. On the other hand, for the gravel beach the three models (Figure 7) show very similar results. In particular they all show a similar degree of accuracy in the backwash, even at a later stage.

24

As discussed in Section 2.1.1, description of the evolution of the TKE is one of the most important capabilities of depth-resolving models. The LES and RANS models use different approaches to do this (see Section 3.1). The two numerical models qualitatively predict the TKE evolution. Numerical results of TKE profiles at two different cross-shore locations (PIV2 and PIV4) are compared against measured data for the gravel case (Figure 8). The TKE profiles at the two locations correspond to: the bore arrival, uprush, near flow reversal, backwash, and late backwash. During bore arrival at PIV2, the TKE profile structure is depth uniform and remains so during the uprush and flow reversal (Figure 8). The TKE structure is well captured by the LES model during these stages, whereas the RANS model overpredicts the observed TKE near the surface. However, the RANS model is able to predict the TKE near the bed. At PIV4 a fully turbulent bore propagates with large TKE near the bed during the uprush. At this location the RANS model better reproduces the experimental data. During the backwash phase the RANS model captures the near bed turbulence that controls the TKE production at this stage. In general, the RANS model tends to overpredict the turbulence in the upper water column, whereas the LES model tends to underpredict turbulence, especially very near the bed (Figure 8).

The LES model allows us to investigate the complex 3D structure of the flow turbulence during the dam-break. Thus, the evolution and fate of turbulent coherent structures are investigated using the λ_2-method (Jeong and Hussain, 1995). The λ_2 is defined as the eigenvalues of the symmetric tensor $S^2 + \omega^2$ with S and ω representing the symmetric and anti-symmetric components of the velocity gradient tensor. By examining the coherent structures, we can deduct that the dam-break driven flow becomes a fully turbulent bore before it reaches the rough slope. Figure 9 presents the instantaneous images of iso-surfaces of $\lambda_2 =$ -700 during the uprush and the backwash. During the uprush, coherent structures are concentrated on the swash front and actively interact with the sloping bed (Figure 9a). On the contrary, during the backwash, they are evenly distributed in the streamwise and spanwise direction (Figure 9b). The shape of

25

the coherent structure obtained during backwash is similar to boundary layer shear generated turbulence.

4.3.2. BBL dynamics

The numerical predictions of the bed shear stress are here compared with those computed from logarithmic profile fitting to the measured velocity profiles. Figures 10 and 12 show that the log-law method predicts that the stress is maximum at the bore arrival and rapidly decreases. As anticipated in Section 2.1.2, the models presented here are able to reproduce the uprush evolution. However, results diverge from experimental estimations during the backwash phase where τ_b increases throughout the backwash at PIV2 (upper panel in Figure 10). Depth-resolving models (i.e., RANS and LES) predict a smaller backwash peak value at this location and the numerical τ_b decreases at a later stage of the backwash. The two depth-resolving models overpredict the bed shear stress magnitude during bore arrival. Consistent with the laboratory data, depth-resolving models predict larger shear stresses for the gravel bed case (not shown). Further up the beach, e.g., at the PIV5 station, the numerical models are in better agreement with respect to data. The LES predicts the bed shear stress evolution during the uprush, whereas the RANS model performance is better during the backwash. The discrepancy between the LES model and the data during the backwash may be caused by relatively coarse vertical grid and simple near wall modelling used in the LES model.

On the other hand, the two depth-integrated approaches used rely on the momentum integral method for the computation of the bed shear stress. This means that τ_b is computed starting from the knowledge of δ. This is shown for PIV4 only in Figure 11. The evolution at other measuring stations is very similar, hence omitted. As explained in Section 2.1.2, δ grows quickly after the bore arrival. The two models mainly differ in the rate at which this growth occurs, with Barnes and Baldock (2010) predicting that $\delta = h$ as the swash tip arrives at these measurement locations, i.e., that the BBL becomes fully developed early in the uprush. The simple momentum integral method predicts that

26

$\delta = 0$ at flow reversal and grows again in backwash. In the backwash although the models differ in the growth rate, they both predict that $\delta = h$ between $1 - 2s$ after flow reversal.

The predicted bed shear stress is presented at PIV2, PIV4 and PIV5 in Figure 12 for both models. The general qualitative description of the evolution of τ_b is good and consistent with the depth-resolving models, above all during the uprush. However, Briganti et al. (2011) model predicts at bore arrival a very high value for τ_b that is equal to 238 N/m^2 at PIV2 and slightly decreases further up the beach, becoming $\tau_b = 180$ N/m^2 at PIV5. The accuracy of models in the backwash deteriorates, compared to the log-law, above all immediately after flow reversal. All models suggest a lower shear stress during the backwash than estimated from the log-law. Conversely, Barnes and Baldock (2010) found that the LBLM overestimated direct bed shear measurements for smooth beds in this same facility. Thus, it is not clear whether the models or the log-law provide the better description of the shear stress in the backwash. The depth-averaged model performance is quite good with respect to depth-resolving models, especially for the seaward locations where the two modelling approaches predict a smaller shear stress during the backwash. However, depth-averaged models predict a significantly higher τ_b at bore arrival with respect to depth-resolving ones. Model intercomparison, in fact, suggests that a simple boundary layer model overestimates the peak shear stress in uprush with respect to more sophisticated depth-resolving models. The two approaches are able to predict an increase in the maximum shear stress magnitude for the gravel beach case (not shown).

4.3.3. Infiltration/exfiltration

Here, the VARANS model is employed to simulate the dam-break driven-swash hydrodynamics on a permeable gravel seabed. The flow infiltration/exfiltration plays an important role in the flow transformation inside the swash zone (see Section 2.1.3). Pintado-Patiño et al. (2015) found that for the COBRAS model a value of effective porosity equal to 0.2 yielded the best agreement with respect

to measured data by Kikkert et al. (2013). Bore propagation at the toe of the beach profile occurs above a saturated bed and hence differences during the up-

745 rush with respect to impermeable seabed results remain small. However, as the bore propagated over the permeable seabed, infiltration induces a thinning of the swash lens and saturation of the beach (Figures 13). During the backwash phase flow divergence occurs in the subsurface flow and exfiltration plays an important role in the flow during this stage. The velocity magnitude in the sub-

750 surface flow is an order of magnitude smaller with respect to the surface flow. The infiltration reduces the run-up distance and modulates the BBL evolution (see Pintado-Patiño et al., 2015).

4.3.4. Morphodynamics

Although the laboratory experiments considered here are carried out on a

755 fixed bed, it is possible to show the capabilities of hydro-morpho-dynamic models by using the same setup but allowing the bed to change during the swash event. Both Briganti et al. (2012) and Postacchini et al. (2012) models are used for the bed evolution modeling for the coarse sand case. Given the sediment size, only the bed load is considered. The simulated bed changes with respect

760 to the original profile of the sloping beach (Δz_b) during four stages of the swash event are shown in Figure 14. At $t = 2.59$ s, in the early stage of run-up, the two models predict a sediment bore in correspondence of the tip of the swash lens, while at $t = 5.56$ s, i.e. at the maximum run-up, erosion is present at the toe of the slope, while accretion is shown in the upper beach. At the early stages of the

765 backwash ($t = 6.59$ s) the models predict different bed profiles, while the differences in water depth and shoreline location are small. However, towards the end of the swash event ($t = 9.56$ s), both models predict erosion in the lower part of the beach but differ significantly on the bed evolution at the upper part of the profile. Briganti et al. (2012) predicts that a bed step is formed approximatively

770 at the location of the shoreline before the dam-break ($x = 0$). This is generated by the backwash bore that forms as the backwash progresses as predicted by Zhu and Dodd (2015) for a solitary wave and described in Section 2.2.2. The

28

model also predicts a region of significant erosion shoreward the step. However, for $x > 3.0$ m accretion is observed. Also, Postacchini et al. (2012) predicts the formation of a bed step, which is larger than that predicted by Briganti et al. (2012). A wider region of erosion with a slightly deeper maximum is observed shoreward the step. The upper part of the beach is characterised by an area of erosion with accretion only found in the upper limit of the swash zone.

Clearly, in absence of measurements it is not possible to assess the accuracy of the models and hence only the relative differences and similarities can be discussed. Several factors may contribute to the different results. The two models solve the governing equations using two different numerical schemes, they also interpret the coupling between NLSWE in two different ways, as outlined in the previous paragraph. Moreover, the two models rely on two different shoreline boundary conditions. Interestingly, features such as the formation of a bed step are present in both a fully coupled and a weakly coupled model, as already partially demonstrated in Postacchini et al. (2012).

5. Discussion

The results shown in the previous section allow a discussion on the performance and capabilities of the different state-of-the-art numerical models here presented. First, it has to be noted that the computational time for a dam-break driven (single) swash event of 10 seconds depends on the degree of the sophistication in the numerical models, ranging from $O(1)$ minutes in NLSWE, $O(1)$ hours in the RANS model, and $O(10)$ days in the LES model. Therefore, the selection of the numerical model is strongly dependent on the processes of interest.

In order to quantitatively assess models performance the model skill value is estimated as (Willmott et al., 1985),

$$\theta_{skill} = 1 - \left[\frac{\sum\limits_{t_{ini}}^{t_{end}} (\theta_{pred,t} - \theta_{meas,t})^2}{\sum\limits_{t_{ini}}^{t_{end}} \left(|\theta_{pred,t} - \overline{\theta_{meas,t_{ini:end}}}| + |\theta_{meas,t} - \overline{\theta_{meas,t_{ini:end}}}| \right)^2} \right], \quad (8)$$

where θ_{pred} and θ_{meas} represent the predicted and measured quantity from the first (t_{ini}) to the last (t_{end}) measurement time. The model skill ranges from complete disagreement ($\theta_{skill} = 0$) to perfect agreement ($\theta_{skill} = 1$). Furthermore, the model performance is also evaluated using the root-mean-squared error (RMSE) given by,

$$RMSE = \sqrt{\frac{\sum_{t_{ini}}^{t_{end}} (\theta_{meas,t} - \theta_{pred,t})^2}{n_{steps}}}, \qquad (9)$$

where n_{steps} is the total number of time steps between t_{ini} and t_{end}. Table 3 presents both the model skill and the RMSE for the shoreline position, h and U for the two simulated cases (i.e., sand and gravel). Notice that θ_{skill} and RMSE for h and U correspond to the averaged value over PIV2 to PIV6 locations. All the models considered in our benchmarking produce a fairly accurate description of h and U during the swash event. Best performance is obtained for h by all models, while for U and above all for x_s larger values of $RMSE$ are found. Differences in x_s with respect to data are less significant during the run-up phase than in the backwash. At this stage of the flow the models' accuracy deteriorates and, for the depth integrated models, the performance seems to depend on the closure used for τ_b. This might be critical for the correct modelling of swash-swash interactions under realistic conditions. In general, depth-resolving models provided a better description of the flow during the backwash, at a high computational cost. Note that, in these experiments the bed is very rough, given the flow depths present, in comparison to sandy beaches at least, and therefore the experiments represent challenging conditions. Similarly, for U the performance is very similar for all models during uprush, while the performance depends on how well backwash velocity are modelled.

The modelling of τ_b in depth-integrated models has progressed significantly in ten years. Although Chezy and Manning approaches are still very common, more physically-based models have been proposed. However, it is still difficult to assess the accuracy of the proposed closures for τ_b at critical stages of the flow evolution. This is mainly due to difficulties in the measurements of the

30

highly aerated turbulent bore. For instance, uncertainty still exists on the values of τ_b in the bore front and during the backwash, where the estimate of τ_b from data is more difficult. Furthermore, discrepancies between the log-law estimates and direct bed shear measurements (e.g., Barnes and Baldock, 2010) in the same facility have been noted by Kikkert et al. (2012). The depth-resolving models satisfactorily represent the bed shear stress evolution and only rely on the definition of the apparent bed roughness. Furthermore, their capability to simulate the velocity and turbulence field allow investigation of the applicability of boundary layer models inside the swash zone.

Turbulence modelling within the swash zone is difficult even for LES models. The LES and RANS model are able to partially predict the TKE evolution during the dam-break driven swash at different locations. The TKE values predicted by the LES model are in better agreement with respect to data near the surface, whereas the RANS model performance is better for the near bed values. This deficiency in the LES model may be due to the uncertainties in near wall modelling, due to insufficient vertical resolution near the bed. However, to avoid near-wall modelling, much higher resolution is needed (e.g., Germano et al., 1991), which is not affordable in the present study . Appropriate near-wall models for LES model in swash zone deserves further investigation. Despite the simplified $\kappa - \epsilon$ closure the RANS model performance is reliable for predicting the turbulence-averaged flow velocities with a relatively low computational cost. However, a LES model is required in order to investigate turbulent coherent structures that may contribute significantly to sediment transport. An important issue to resolve in the coming decade is whether the current state of the art in sediment transport modelling warrants the use of depth-resolving models (and turbulence modelling) for practical use.

The infiltration and exfiltration is believed to play an important role in boundary layer dynamics, sediment transport, and run-up, but this is yet to be verified experimentally. For example, it is clear that the infiltration influences the run-up and flow velocity, which would have direct consequences for sediment transport. Nevertheless, it is less clear how the infiltration or exfiltration affect

31

sediment transport directly (see Baldock and Nielsen, 2010, for a discussion). It appears that numerical models have now advanced to a stage to provide sufficiently accurate estimates of the hydrodynamics that they can provide useful tools to investigate these issues. The results from the depth-resolving model are consistent with observations in laboratory experiments on a permeable bed. However, this approach is only suitable for coarse sediment and, hence, needs to be extended for modelling sand beds. It is also anticipated that future contributions may come from similar efforts under multiphase-coupled resolving models that incorporate air effects and pore pressure build up at the bed interface. Furthermore, the effect of infiltration and exfiltration on beach morphology evolution is still an open subject for future numerical based research.

The capabilities of hydro- morphodynamic models in the last ten years have increased remarkably. The fundamental response of the governing equations has been understood. Most importantly, a number of idealised swash events has been studied and a few quasi-analytical solutions have been derived, therefore it is possible to understand theoretical differences between different approaches. However, the lack of intra-swash measurements of the morphodynamics during the event makes it impossible to assess in detail the accuracy of the description of the bed evolution. Future work should consider further model-data comparisons of the form presented by Postacchini et al. (2014), where total sediment transport rates obtained from overtopping experiments are very reliable. Notwithstanding the evolution of the morphodynamics models, there is a staggering mismatch between the complexity of the description of the flow and that of the bed behaviour. Models still rely on classical formulations of sediment transport that do not take into account the unsteady nature of the swash motion and, in turn, the different sediment transport modes that occur during a swash event such as the sheet flow transport. An accurate assessment of the capability of numerical models to describe intra-swash sediment transport in field conditions has not been carried out yet. Also, some numerical aspects, such as the role of the shoreline boundary conditions in the description of the bed evolution, need to be clarified. As noted above, considerable uncertainties exist

32

in sediment transport models, even for simple parameters such as the influence of grain size (Othman et al., 2014).

6. Conclusions

₈₉₅ A review of the state-of-the art of numerical modelling of swash zone processes is presented, together with a critical assessment of the performance of a range of numerical models against a comprehensive data set. Depth-averaged models are well established and provide practical tools for engineering use for modelling short duration wave-by-wave events and the study of beach evolu-₉₀₀tion. Additional refinements such as coupling between hydrodynamics and bed morphology have recently been introduced. Further refinements could include coupling of boundary layer models and including sheet-flow sediment transport models. On the other hand, depth-resolving RANS and LES models provide improved predictions of both the mean and turbulence components of the flow at ₉₀₅significant extra computational cost. Swash zone modelling is limited due to the current limitations for obtaining reliable measurements within the swash such as the bed shear stresses and intra-wave bed morphology changes. For instance, the significance of the differences between the depth-averaged models and the depth-resolving models in terms of prediction of bed shear stress is not clear, ₉₁₀since the present data set is based on log-law estimates of bed shear stress which have some uncertainty. The trend and magnitude of the shear stress predicted by all models is reasonable, particularly in the uprush. However, further data is needed for shear stress, sediment transport, and beach morphology changes to determine if this additional effort is warranted for sediment transport mod-₉₁₅elling. This poses the problem of quantity and quality of data. Existing field measurements are difficult to study numerically because the numerical setup (e.g., offshore, boundary conditions, initial conditions for hydrodynamic and sediment transport quantities) was not considered or not available when these measurements were planned. A better synergy between the numerical and field

33

Table 1: Experimental sediment characteristics.

Diameters [mm]	1.5 mm coarse sand	6.0 mm gravel	10 mm gravel
D_{50}	1.3	5.4	8.4

Table 2: Positions of the centre of the PIV/LIF measurement stations.

Station	x[m]
PIV1	-1.802
PIV2	0.072
PIV3	0.769
PIV4	1.559
PIV5	2.365
PIV6	3.161

Table 3: Models skill θ_{skill} and RMSE (in parenthesis) for the shoreline position x_s, water depth h, and depth-averaged velocity U for the sand and gravel beach cases.

Variable	LES	RANS	Briganti et al. (2011)	ANUGA	Postacchini et al. (2012)
			D_{50}=1.5 mm		
x_s	0.97	0.98	0.99	0.94	0.99
	(0.52 m)	(0.34 m)	(0.22 m)	(0.76 m)	(0.33 m)
h	0.95	0.99	0.99	0.95	0.98
	(0.012 m)	(0.006 m)	(0.004 m)	(0.012 m)	(0.004 m)
U	0.99	0.99	0.98	0.98	0.99
	(0.14 m/s)	(0.07 m/s)	(0.20 m/s)	(0.15 m/s)	(0.13 m/s)
			D_{50}=6.0 mm		
x_s	0.87	0.99	0.97	0.81	0.94
	(0.96 m)	(0.11 m)	(0.47 m)	(1.05 m)	(0.62 m)
h	0.94	0.98	0.98	0.94	0.98
	(0.164 m)	(0.008 m)	(0.007 m)	(0.013 m)	(0.006 m)
U	0.98	0.99	0.98	0.98	0.99
	(0.16 m/s)	(0.09 m/s)	(0.13 m/s)	(0.12 m/s)	(0.10 m/s)

Figure 1: Sketch of variables for a generic one-dimensional swash event on a mobile bed.
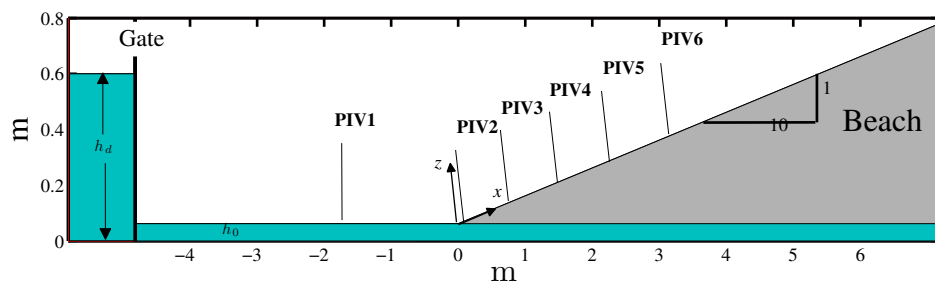
Figure 2: Sketch of the experimental setup.
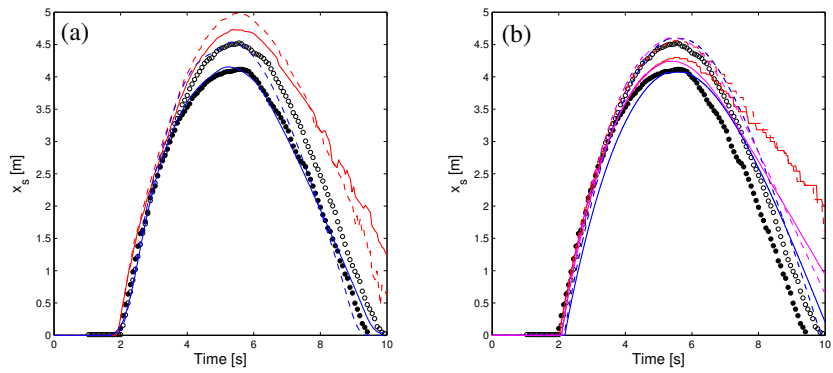
Figure 3: (a) Shoreline trajectory for depth-resolving models during the swash event for the coarse sand beach (Data: open circles; RANS: blue dashed line; LES: red dashed line) and for the 6.0 mm gravel beach (Data: filled circles; RANS: blue solid line; LES: red solid line). (b) Shoreline trajectory for depth-averaged models during the swash event for the coarse sand beach (Data: open circles; Briganti et al. (2011): blue dashed line; ANUGA: red dashed line; Postacchini et al. (2012): magenta dashed line) and for the 6.0 mm gravel beach (Data: filled circles; Briganti et al. (2011): blue solid line; ANUGA: red solid line; Postacchini et al. (2012): magenta solid line).
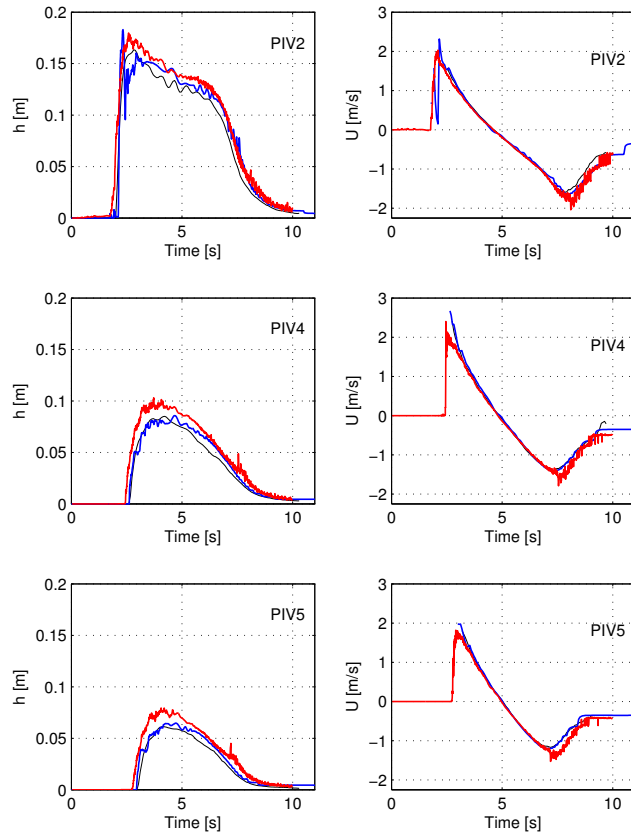
Figure 4: Numerical and experimental results for the coarse sand beach. Left column: time series of water depth (Data: black solid line; RANS model: blue solid line; LES: red solid line) at PIV2, PIV4, and PIV5 for the sand beach. Right column: time series of depth-averaged velocity (Data: black solid line; RANS model: blue solid line; LES: red solid line) at PIV2, PIV4, and PIV5 for the sand beach.
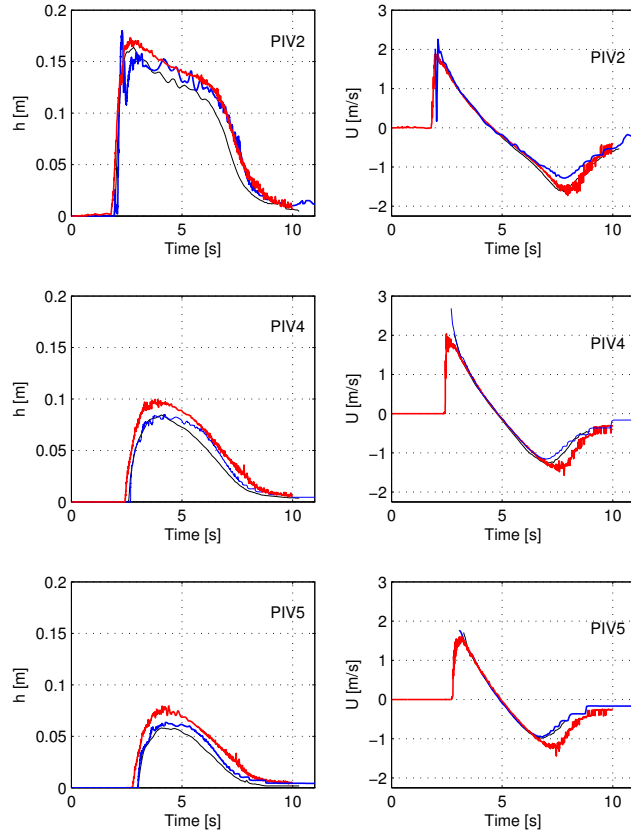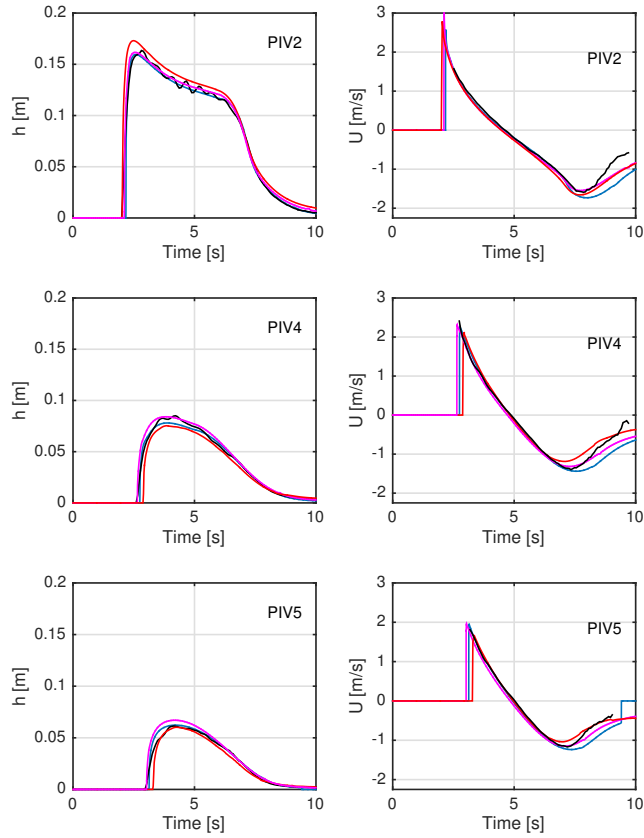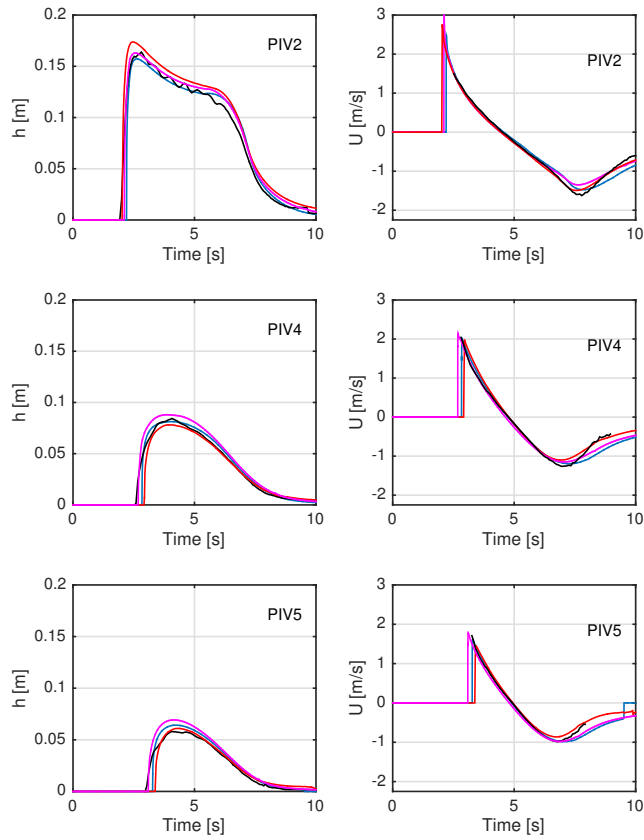
Figure 5: Numerical and experimental results for the 6.0 mm gravel beach. Left column: time series of water depth (Data: black solid line; RANS model: blue solid line; LES: red solid line) at PIV2, PIV4, and PIV5 for the gravel beach. Right column: time series of depth-averaged velocity (Data: black solid line; RANS model: blue solid line; LES: red solid line) at PIV2, PIV4, and PIV5 for the gravel beach.

41

Figure 6: Numerical and experimental results for the coarse sand beach. Left column: time series of water depth (Data: black solid line; Briganti et al. (2011): blue solid line; ANUGA-LBLM: red solid line, Postacchini et al. (2012): magenta) at PIV2, PIV4 and PIV5 for the sand beach. Right column: time series of depth-averaged velocity (Data: black solid line; Briganti et al. (2011): blue solid line; ANUGA-LBLM: red solid line; Postacchini et al. (2012): magenta solid line) at PIV2, PIV4 and PIV5 for the sand beach.

Figure 7: Numerical and experimental results for the 6.0 mm gravel beach. Left column: time series of water depth (Data: black solid line; Briganti et al. (2011): blue solid line; ANUGA-LBLM: red solid line, Postacchini et al. (2012) at PIV2, PIV4 and PIV5 for the sand beach. Right column: time series of depth-averaged velocity (Data: black solid line; Briganti et al. (2011): blue solid line; ANUGA-LBLM: red solid line; Postacchini et al. (2012): magenta solid line) at PIV2, PIV4 and PIV5 for the sand beach.
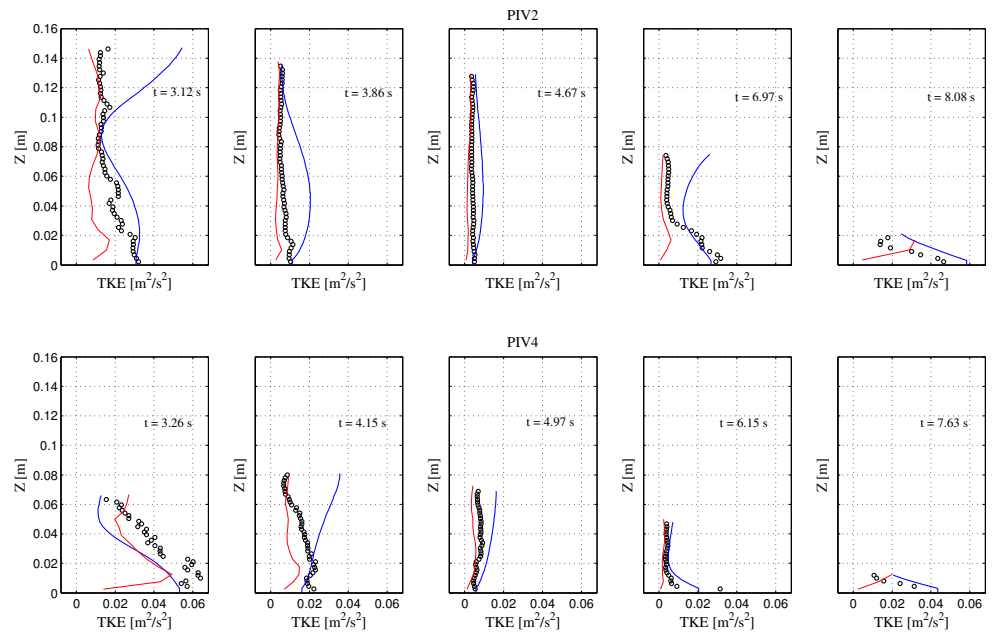
Figure 8: Numerical (RANS: blue solid line; LES: red solid line) and experimental (open cirlces) Turbulent Kinetic Energy (TKE) profiles at PIV2 (upper panels) and PIV4 (lower panels) during different swash phases, bore arrival, uprush, near flow reversal, backwash, and late backwash.
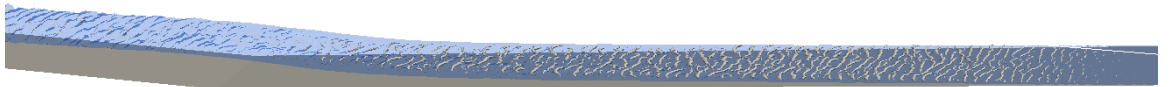
44
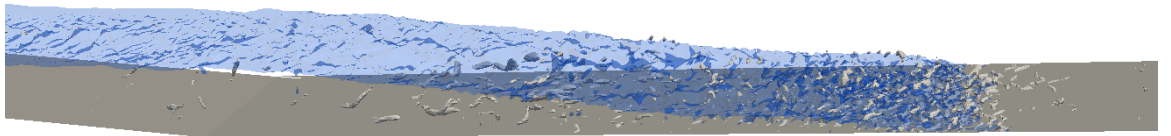
Figure 9: Coherent structures for the gravel case during (a) Uprush, t=2.5 sec, $\lambda_2 = -700$, (b) Downwash, t=7.0 s, $\lambda_2 = -700$.
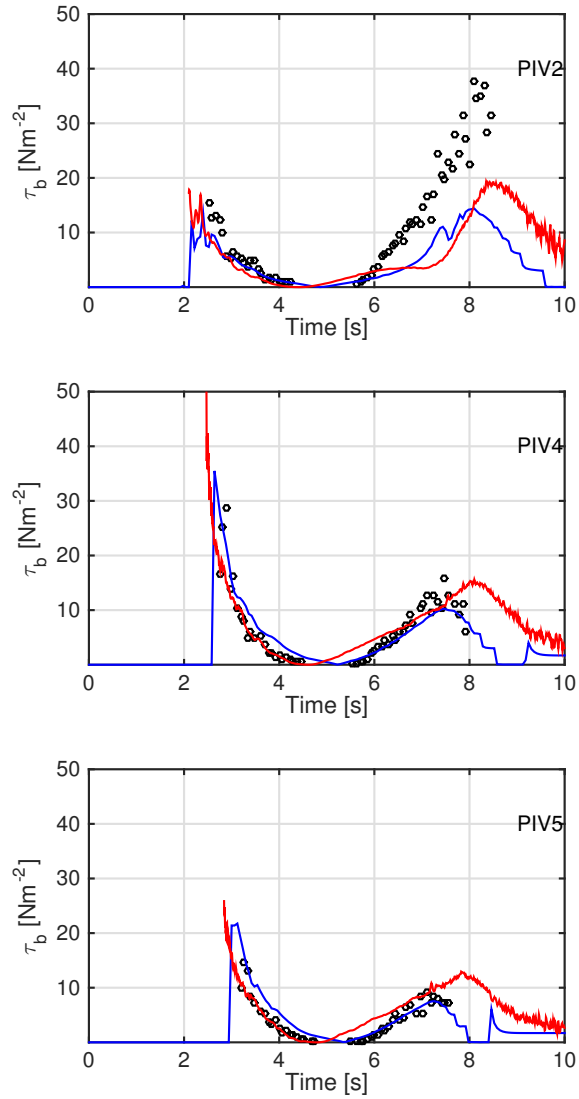
Figure 10: Time series of bed shear stress (Data: open circles; RANS: blue solid line; LES: red solid line) at PIV2, PIV4 and PIV5 for the coarse sand beach.
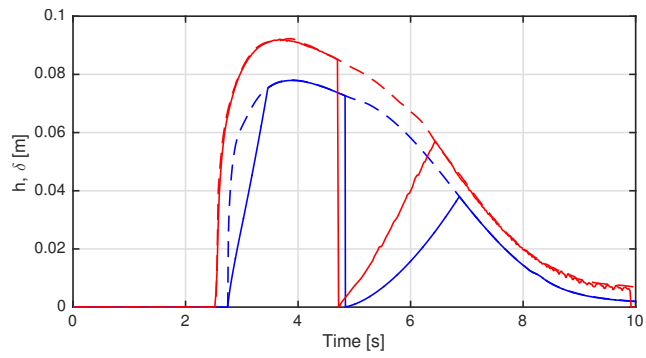
46

Figure 11: Evolution of the boundary layer thickness (δ) (Briganti et al. (2011): blue solid line; ANUGA: red solid line) and h (Briganti et al. (2011): blue dashed line; ANUGA: red dashed line) at PIV4 for the coarse sand beach.
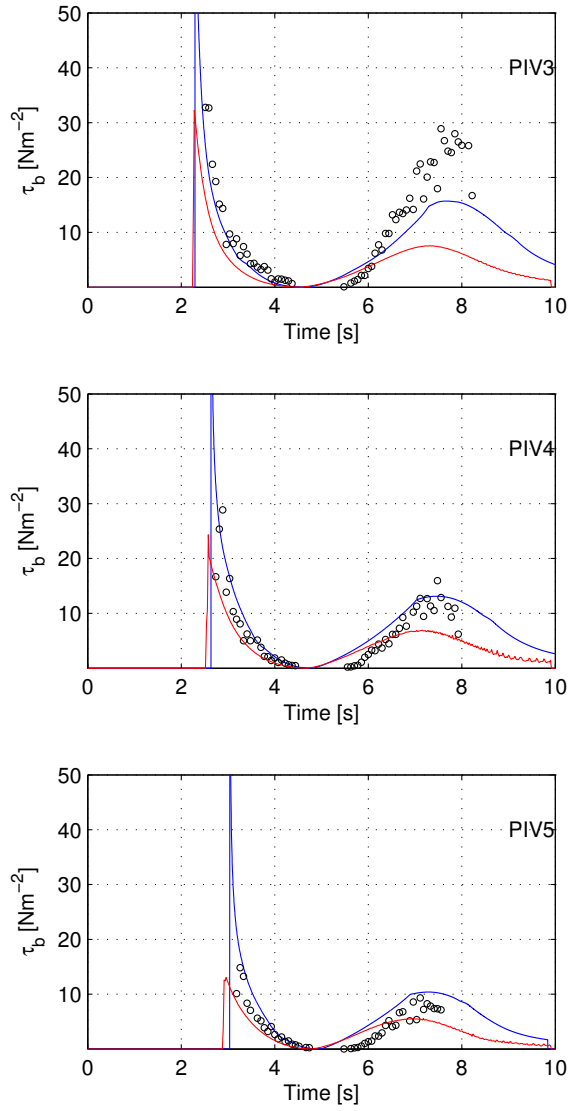
Figure 12: Time series of bed shear stress (Data: open circles Briganti et al. (2011): blue solid line; ANUGA: red solid line) at PIV2, PIV4 and PIV5 for the coarse sand beach. Note that at bore arrival Briganti et al. (2011) is above the range of the τ_b axis of the panels at all three measurement stations.
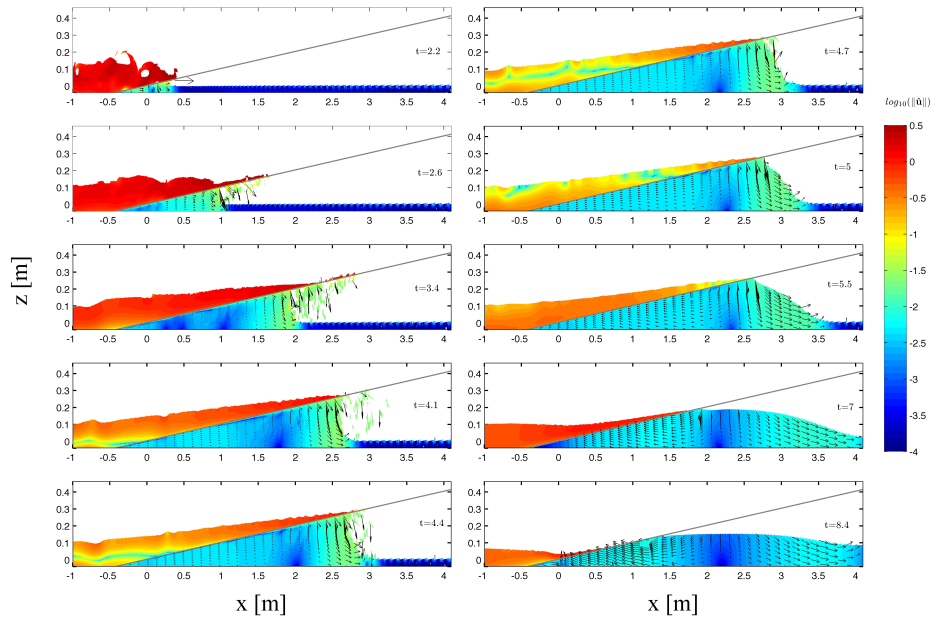
Figure 13: Spatio-temporal distribution of the velocity magnitude in the surface and subsurface flow during different times of the swash cycle. The velocity magnitude is represented in logarithmic scale for visualizing purposes.
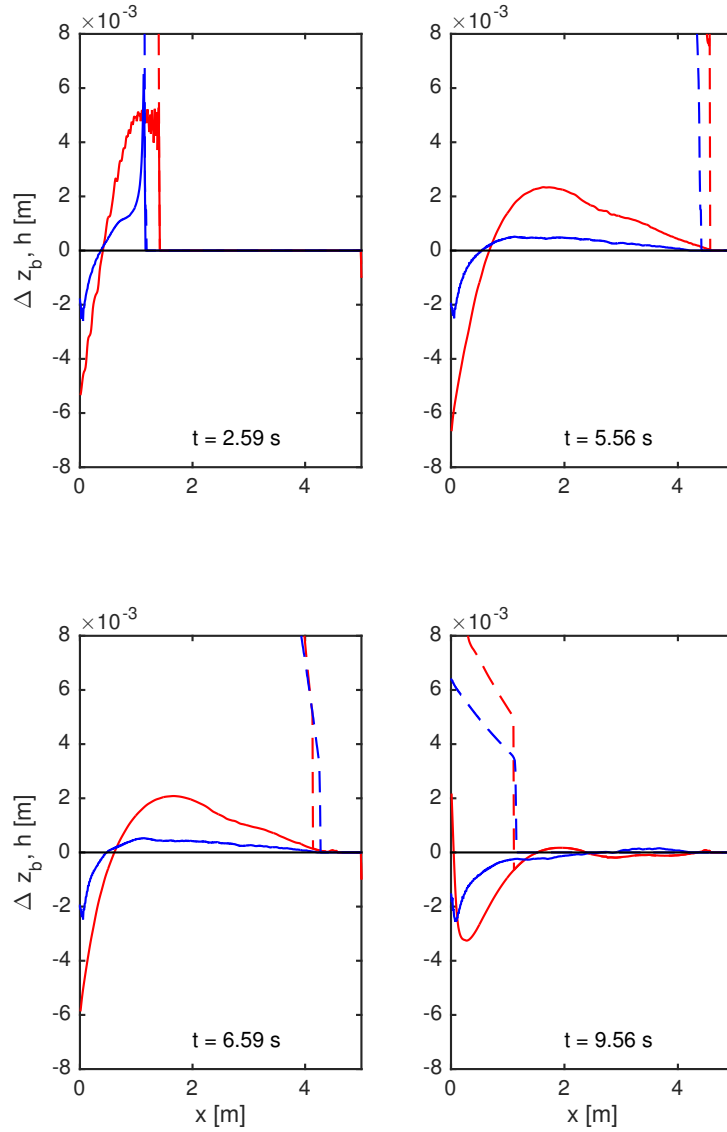
49

Figure 14: Comparison between Δz_b (solid lines) and h (dashed lines), during four stages of the swash event under study: $t = 2.5925$ s, early stage of run-up, $t = 5.5555$ s, maximum run-up, $t = 6.5924$ s early stage of backwash and $t = 9.5555$ s late stage of backwash: Briganti et al. (2012) (blue lines) and Postacchini et al. (2012) (red lines).

References

Alsina, J.M., Falchetti, S., Baldock, T.E., 2009. Measurements and modelling of the advection of suspended sediment in the swash zone by solitary waves. Coastal Engineering 56, 621 – 631. doi:http://dx.doi.org/10.1016/j.coastaleng.2009.01.007.

Amoudry, L., Hsu, T.J., Liu, P.L.F., 2008. Two-phase model for sand transport in sheet flow regime. J. Geophys. Res. 113, 287.

Amoudry, L.O., Liu, P.L.F., 2010. Parameterization of near-bed processes under collinear wave and current flows from a two-phase sheet flow model. Continental Shelf Research 30, 1403 – 1416. doi:http://dx.doi.org/10.1016/j.csr.2010.04.009.

Bakhtyar, R., Barry, D., Yeganeh-Bakhtiary, A., Ghaheri, A., 2009. Numerical simulation of surfswash zone motions and turbulent flow. Advances in Water Resources 32, 250 – 263. doi:http://dx.doi.org/10.1016/j.advwatres.2008.11.004.

Bakhtyar, R., Brovelli, A., Barry, D., Li, L., 2011. Wave-induced water table fluctuations, sediment transport and beach profile change: Modeling and comparison with large-scale laboratory experiments. Coastal Engineering 58, 103 – 118. doi:http://dx.doi.org/10.1016/j.coastaleng.2010.08.004.

Baldock, T., Kudo, A., Guard, P., Alsina, J., Barnes, M., 2008. Lagrangian measurements and modelling of fluid advection in the inner surf and swash zones. Coastal Engineering 55, 791 – 799. doi:http://dx.doi.org/10.1016/j.coastaleng.2008.02.013.

Baldock, T., Nielsen, P., 2010. Discussion of effect of seepage-induced nonhydrostatic pressure distribution on bed-load transport and bed morphodynamics by Simona Francalanci, [g]ary [p]arker, and [l]uca Solari. ASCE J. Hydraulic Eng. 136, 77–78.

Barnes, M., Baldock, T., 2010. A lagrangian model for boundary layer growth and bed shear stress in the swash zone. Coastal Eng. 57, 385–396.

Berberovi, E., Van Hinsberg, N., Jakirli, S., Roisman, I., Tropea, C., 2009. Drop impact onto a liquid layer of finite thickness: Dynamics of the cavity evolution. Physical Review E - Statistical, Nonlinear, and Soft Matter Physics 79. doi:`10.1103/PhysRevE.79.036306`. cited By 84.

Besio, G., Blondeaux, P., Frisina, P., 2003. A note on tidally generated sand waves. J. Fluid Mech. 485, 171–190, doi:10.1017/S0022112003004415.

Briganti, R., Dodd, N.and Kelly, D., Pokrajac, D., 2012. An efficient and flexible solver for the simulation of the morphodynamics of fast evolving flows on coarse sediment beaches. International Journal for Numerical Methods in Fluids 69(4), 859–877.

Briganti, R., Dodd, N.and Pokrajac, D., O'Donoghue, T., 2011. Non linear shallow water modelling of bore-driven swash: Description of the bottom boundary layer. Coastal Eng. 58(6), 463–477.

Briganti, R., Dodd, N., 2009. Shoreline motion in nonlinear shallow water coastal models. Coastal Eng. 56(5-6), 495–505.

Brocchini, M., Baldock, T., 2008. Recent advances in modeling swash zone dynamics: Influence of surf-swash interaction on nearshore hydrodynamics and morphodynamics. Reviews of Geophysics 46. doi:`10.1029/2006RG000215`. cited By 49.

Brocchini, M., Bernetti, R., Mancinelli, A., Albertini, G., 2001. An efficient solver for nearshore flows based on the WAF method. Coastal Eng. 43, 105–129.

Brocchini, M., Dodd, N., 2008. Nonlinear shallow water equation modeling for coastal engineering. ASCE J. Water. Port Coast. Ocean Eng. 134(2), 104–120.

Calantoni, J., Puleo, J.A., Holland, K.T., 2006. Simulation of sediment motions using a discrete particle model in the inner surf and swash-zones. Continental Shelf Research 26, 610 – 621. doi:`http://dx.doi.org/10.1016/j.csr.2005.11.013`. swash-Zone Processes 1st International Workshop on Swash-Zone Processes.

Chardón-Maldonado, P., Pintado-Patino, J.C., Puleo, J.A., 2016. Advances in swash-zone research: Small-scale hydrodynamic and sediment transport processes. Coastal Engineering doi:`http://dx.doi.org/10.1016/j.coastaleng.2015.10.008`. in Peess.

Desombre, J., Morichon, D., Mory, M., 2013. {RANS} v2f simulation of a swash event: Detailed flow structure. Coastal Engineering 71, 1 – 12. doi:`http://dx.doi.org/10.1016/j.coastaleng.2012.07.001`.

Engelund, F., 1966. Hydraulic resistance of alluvial streams. ASCE J. Hydraulic Eng. 92, 315–326.

Garcia-Navarro, P., Alcrudo, F., Saviron, J., 1992. 1d open channel flow simulation using TVD McCormack scheme. ASCE J. Hydraulic Eng. 118, 1359–1372.

Germano, M., Piomelli, U., Moin, P., Cabot, W., 1991. A dynamic subgrid-scale eddy viscosity model. Physics of Fluids A 3, 1760–1765.

Guard, P., Baldock, T., 2007. The influence of seaward boundary conditions on swash zone hydrodynamics. Coastal Engineering 54, 321 – 331. doi:`http://dx.doi.org/10.1016/j.coastaleng.2006.10.004`.

Hibberd, S., Peregrine, D., 1979. Surf and run-up on a beach: a uniform bore. Journal of Fluid Mechanics 95, 323–345.

Hirt, C.W., Nichols, B.D., 1981. Volume of fluid (VOF) method for the dynamics of free boundaries. Journal of Computational Physics 39, 201–225. doi:`10.1016/0021-9991(81)90145-5`.

Hoque, M.A., Asano, T., 2007. Numerical study on wave-induced filtration flow across the beach face and its effects on swash zone sediment transport. Ocean Engineering 34, 2033–2044. URL: http://www.sciencedirect.com/science/article/pii/S002980180700100X, doi:10.1016/j.oceaneng.2007.02.004.

Hsu, T.J., Hanes, D.M., 2004. Effects of wave shape on sheet flow sediment transport. Journal of Geophysical Research: Oceans 109, n/a–n/a. doi:10.1029/2003JC002075.

Hsu, T.J., Raubenheimer, B., 2006. A numerical and field study on inner-surf and swash sediment transport. Continental Shelf Research 26, 589 – 598. doi:http://dx.doi.org/10.1016/j.csr.2006.02.004. swash-Zone Processes 1st International Workshop on Swash-Zone Processes.

Hsu, T.J., Sakakiyama, T., Liu, P.L.F., 2002. A numerical model for wave motions and turbulence flows in front of a composite breakwater. Coastal Engineering 46, 25–50. doi:10.1016/S0378-3839(02)00045-5.

Hu, P., Li, W., He, Z., Phtz, T., Yue, Z., 2015. Well-balanced and flexible morphological modeling of swash hydrodynamics and sediment transport. Coastal Eng. 96, 27 – 37. URL: http://www.sciencedirect.com/science/article/pii/S0378383914001987, doi:http://dx.doi.org/10.1016/j.coastaleng.2014.10.010.

Incelli, G., Zhu, F., Blenkinsopp, C., Dodd, N., Briganti, R., 2015. Modelling swash morphodynamics at truc vert. In Press, This Issue.

Jeong, J., Hussain, F., 1995. On the identification of a vortex. Journal of Fluid Mechanics 285, 69–94. Cited By 2143.

Karambas, T.V., 2003. Modelling of infiltration-exfiltration effects of cross-shore sediment transport in the swash zone. Coast. Eng. J. 45, 63–82. doi:10.1142/S057856340300066X.

Karambas, T.V., 2006. Prediction of sediment transport in the swash-zone by using a nonlinear wave model. Continental Shelf Research 26, 599 – 609. doi:http://dx.doi.org/10.1016/j.csr.2006.01.014. swash-Zone Processes 1st International Workshop on Swash-Zone Processes.

Kelly, D.M., Dodd, N., 2009. Floating grid characteristics method for unsteady flow over a mobile bed. Computers and Fluids 38, 899–909.

Kelly, D.M., Dodd, N., 2010. Beach-face evolution in the swash zone. J. Fluid Mech. 661(12), 316–340.

Kikkert, G., O'Donoghue, T., Pokrajac, D., Dodd, N., 2012. Experimental study of bore-driven swash hydrodynamics on impermeable rough slopes. Coastal Engineering 60, 149 – 166. doi:http://dx.doi.org/10.1016/j.coastaleng.2011.09.006.

Kikkert, G., Pokrajac, D., O'Donoghue, T., Steenhauer, K., 2013. Experimental study of bore-driven swash hydrodynamics on permeable rough slopes. Coastal Engineering 79, 42 – 56. doi:http://dx.doi.org/10.1016/j.coastaleng.2013.04.008.

Kim, D.H., 2015. H2D morphodynamic model considering wave, current and sediment interaction. Coastal Eng. 95, 27 – 34. doi:http://dx.doi.org/10.1016/j.coastaleng.2014.09.006.

Klostermann, J., Schaake, K., Schwarze, R., 2013. Numerical simulation of a single rising bubble by vof with surface compression. International Journal for Numerical Methods in Fluids 71, 960–982. doi:10.1002/fld.3692. cited By 3.

Lin, P., Liu, P.L.F., 1998a. A numerical study of breaking waves in the surf zone. J. Fluid Mech. 359, 239–264.

Lin, P., Liu, P.L.F., 1998b. Turbulence transport, vorticity dynamics, and solute mixing under plunging waves in surf zones. J. Geophys. Res. 103, 15,677–15,694.

Liu, P.L.F., Lin, P., Chang, K., Sakakiyama, T., 1999. Numerical modeling of wave interaction with porous structures. Journal of Waterway, Port, Coastal, and Ocean Engineering 125, 322–330. doi:`10.1061/(ASCE)0733-950X(1999) 125:6(322)`.

Losada, I.J., Lara, J.L., Guanche, R., González-Ondina, J.M., 2008. Numerical analysis of wave overtopping of high mound breakwaters. Coastal Eng. 55, 47–62. doi:`10.1016/j.coastaleng.2007.06.003`.

McCall, R., Masselink, G., Poate, T., Roelvink, J., Almeida, L., 2015. Modelling the morphodynamics of gravel beaches during storms with XBeach-G. Coastal Engineering 103, 52 – 66. URL: `http://www.sciencedirect. com/science/article/pii/S0378383915001052`, doi:`http://dx.doi.org/ 10.1016/j.coastaleng.2015.06.002`.

Meneveau, C., Katz, J., 2000. Scale-invariance and turbulence models for large-eddy simulation. Annual Review of Fluid Mechanics 32, 1–31. Cited By 589.

Nakayama, A., Kuwahara, F., 1999. A macroscopic turbulence model for flow in a porous medium. J. Fluids Eng. 121, 427–433. doi:`10.1115/1.2822227`.

Nielsen, O., Roberts, S., Gray, D., McPherson, A., Hitchman, A., 2005. Hydrodynamic modelling of coastal inundation, The University of Melbourne, Melbourne, Australia. pp. 518–523.

Nwogu, O.G., 1993. Alternative form of Boussinesq equations for nearshore wave propagation. ASCE J. Water. Port Coast. Ocean Eng. 119, 618–638.

O'Donoghue, T., Pokrajac, D., Hondebrink, L., 2010. Laboratory and numerical study of dambreak-generated swash on impermeable slopes. Coastal Engineering 57, 513 – 530. doi:`http://dx.doi.org/10.1016/j.coastaleng. 2009.12.007`.

Othman, I.K., Baldock, T.E., Callaghan, D.P., 2014. Measurement and modelling of the influence of grain size and pressure gradient on swash uprush

sediment transport. Coastal Engineering 83, 1 – 14. doi:`http://dx.doi.org/10.1016/j.coastaleng.2013.09.001`.

Pedrozo-Acuna, A., Simmonds, D., Otta, A., Chadwick, A., 2006. On the cross-shore profile change of gravel beaches. Coastal Eng. 53, 335–347. doi:`10.1016/j.coastaleng.2005.10.019`. cited By 50.

Pedrozo-Acuña, A., Simmonds, D.J., Chadwick, A.J., Silva, R., 2007. A numerical–empirical approach for evaluating morphodynamic processes on gravel and mixed sand–gravel beaches. Marine Geology 241, 1–18.

Peregrine, D., Williams, S.M., 2001. Swash overtopping a truncated beach. J. Fluid Mech. 440, 391–399.

Pintado-Patiño, J.C., Torres-Freyermuth, A., Puleo, J.A., Pokrajac, D., 2015. On the role of infiltration and exfiltration in swash zone boundary layer dynamics. Journal of Geophysical Research: Oceans 120, 6329–6350. URL: `http://dx.doi.org/10.1002/2015JC010806`, doi:`10.1002/2015JC010806`.

Postacchini, M., Brocchini, M., Mancinelli, A., Landon, M., 2012. A multi-purpose, intra-wave, shallow water hydro-morphodynamic solver. Advances in Water Resources 38, 13 – 26. URL: `http://www.sciencedirect.com/science/article/pii/S0309170811002326`, doi:`http://dx.doi.org/10.1016/j.advwatres.2011.12.003`.

Postacchini, M., Othman, I., Brocchini, M., Baldock, T., 2014. Sediment transport and morphodynamics generated by a dam-break swash uprush: Coupled vs uncoupled modeling. Coastal Eng. 89, 99–105. URL: `http://www.scopus.com/inward/record.url?eid=2-s2.0-84899862297&partnerID=40&md5=15af7be0bb12ec8e1bcefc1153c28e5f`, doi:`10.1016/j.coastaleng.2014.04.003`. cited By 1.

Pritchard, D., Hogg, A.J., 2005. On the transport of suspended sediment by a swash event on a plane beach. Coastal Engineering 52, 1 – 23. doi:`http://dx.doi.org/10.1016/j.coastaleng.2004.08.002`.

Puleo, J.A., Butt, T., 2006. The first international workshop on swash-zone processes. Continental Shelf Research 26, 556 – 560. doi:`http://dx.doi.org/10.1016/j.csr.2006.01.008`. swash-Zone Processes 1st International Workshop on Swash-Zone Processes.

Puleo, J.A., Farhadzadeh, A., Kobayashi, N., 2007. Numerical simulation of swash zone fluid accelerations. Journal of Geophysical Research: Oceans 112, n/a–n/a. doi:`10.1029/2006JC004084`.

Puleo, J.A., Lanckriet, T., Wang, P., 2012. Near bed cross-shore velocity profiles, bed shear stress and friction on the foreshore of a microtidal beach. Coastal Engineering 68, 6–16. doi:`10.1016/j.coastaleng.2012.04.007`.

Rusche, H., 2002. Computational fluid dynamics of dispersed two-phase flows at high phase fractions. Ph.D. thesis. Imperial College of Scu. Technol and Med.. London, England.

Shih, T.H., Zhu, J., Lumley, J.L., 1996. Calculation of Wall-Bounded Complex Flows and Free Shear Flows. International Journal for Numerical Methods in Fluids 23, 1133–1144. doi:`10.1002/(SICI)1097-0363(19961215)23:11<1133::AID-FLD456>3.0.CO;2-A`.

Steenhauer, K., Pokrajac, D., O'Donoghue, T., 2012. Numerical model of swash motion and air entrapment within coarse-grained beaches. Coastal Engineering 64, 113 – 126. doi:`http://dx.doi.org/10.1016/j.coastaleng.2012.01.004`.

Ting, F., 2006. Large-scale turbulence under a solitary wave. Coastal Engineering 53, 441–462. doi:`10.1016/j.coastaleng.2005.11.004`.

Ting, F., 2008. Large-scale turbulence under a solitary wave: Part 2. forms and evolution of coherent structures. Coastal Engineering 55, 522–536. doi:`10.1016/j.coastaleng.2008.02.018`.

Tonelli, M., Petti, M., 2012. Shock-capturing boussinesq model for irregular wave propagation. Coastal Engineering 61, 8 – 19. URL: `http:`

//www.sciencedirect.com/science/article/pii/S0378383911001815,
doi:http://dx.doi.org/10.1016/j.coastaleng.2011.11.006.

Toro, E., 1990. Riemann problems and the WAF method for the two-dimensional
shallow water equations. Technical Report UTM 314. University of Trento,
Department of Mathematics.

Torres-Freyermuth, A., Puleo, J.A., Pokrajac, D., 2013. Modeling swash-zone
hydrodynamics and shear stresses on planar slopes using reynolds-averaged
navierstokes equations. Journal of Geophysical Research: Oceans 118, 1019–
1033. doi:10.1002/jgrc.20074.

White, F.M., 2006. Viscous fluid flow. McGraw-Hill Science/Engineering/Math.

Willmott, C.J., Ackleson, S.G., Davis, R.E., Feddema, J.J., Klink, K.M.,
Legates, D.R., O'Donnell, J., Rowe, C.M., 1985. Statistics for the evalua-
tion and comparison of models. Journal of Geophysical Research: Oceans 90,
8995–9005. URL: http://dx.doi.org/10.1029/JC090iC05p08995, doi:10.
1029/JC090iC05p08995.

Xiao, H., Young, Y.L., Provost, J.H., 2010. Hydro- and morpho-dynamic mod-
eling of breaking solitary waves over a fine sand beach. part ii: Numerical sim-
ulation. Marine Geology 269, 119 – 131. URL: http://www.sciencedirect.
com/science/article/pii/S0025322709003259, doi:http://dx.doi.org/
10.1016/j.margeo.2009.12.008.

Zhang, Q., Liu, P.L.F., 2008. A numerical study of swash flows generated by
bores. Coastal Engineering 55, 1113 – 1134. doi:http://dx.doi.org/10.
1016/j.coastaleng.2008.04.010.

Zhou, Z., Sangermano, J., Hsu, T.J., Ting, F.C.K., 2014. A numerical in-
vestigation of wave-breaking-induced turbulent coherent structure under a
solitary wave. Journal of Geophysical Research: Oceans 119, 6952–6973.
doi:10.1002/2014JC009854.

Zhu, F., Dodd, N., 2013. Net beach change in the swash zone: A numerical investigation. Advances in Water Resources 53, 12–22.

Zhu, F., Dodd, N., 2015. The morphodynamics of a swash event on an erodible beach. J. Fluid Mech. 762, 110 – 140.

Zhu, F., Dodd, N., Briganti, R., 2012. Impact of a uniform bore on an erodible beach. Coastal Eng. 60, 326–333.

Zoppou, C., Roberts, S., 1999. Catastrophic collapse of water supply reservoirs in urban areas. ASCE J. Hydraulic Eng. 125, 686–695.